

# High-Order, Finite-Volume Methods in Mapped Coordinates

P. Colella <sup>a,2</sup>, M. R. Dorr <sup>b,1</sup>, J. A. F. Hittinger <sup>b,\*,1</sup>,  
D. F. Martin <sup>a,2</sup>

<sup>a</sup>*Applied Numerical Algorithms Group, Lawrence Berkeley National Laboratory,  
One Cyclotron Road Mail Stop 50A-1148, Berkeley, CA 94720*

<sup>b</sup>*Center for Applied Scientific Computing, Lawrence Livermore National  
Laboratory, 7000 East Avenue L-561, Livermore, CA 94550*

---

## Abstract

We present an approach for constructing finite-volume methods of any order of accuracy for control-volume discretizations of space defined as the image of a smooth mapping from a rectangular discretization of an abstract coordinate space. Our approach is based on two ideas. The first is that of using higher-order quadrature rules to compute the flux averages over faces that generalize a method developed for Cartesian grids to the case of mapped grids. The second is a method for computing the averages of the metric terms on faces such that freestream preservation is automatically satisfied. We derive detailed formulas for the cases of fourth-order accurate discretizations of linear elliptic and hyperbolic partial differential equations; for the latter case, we combine the method so derived with Runge-Kutta time discretization and the new high-order accurate limiter to obtain a method that is robust in the presence of discontinuities and underresolved gradients. For both elliptic and hyperbolic problems, we demonstrate that the resulting methods are fourth-order accurate for smooth solutions.

*Key words:* Finite-volume method, high-order discretization, mapped grids, hyperbolic and elliptic partial differential equations

*1991 MSC:* 65M06, 65M12, 65N06, 65N12, 65N22

---

\* Corresponding author.

*Email addresses:* pcolella@lbl.gov (P. Colella ), dorr1@llnl.gov (M. R. Dorr ), hittinger1@llnl.gov (J. A. F. Hittinger ), dfmartin@llnl.gov (D. F. Martin ).

<sup>1</sup> This work performed under the auspices of the U.S. Department of Energy by Lawrence Livermore National Laboratory under Contract DE-AC52-07NA27344. LLNL-JRNL-422807-DRAFT.

<sup>2</sup> Research supported by the Office of Advanced Scientific Computing Research of

## 1 Introduction

Finite-volume methods are a popular choice for the discretization of partial differential equations involving flux divergences, *e.g.*, conservation laws. In such approaches, the spatial domain is decomposed into a set of control volumes. The boundary of each volume is represented as a union of faces, with each face shared by exactly two control volumes. Based on this discretization of space, the average of the divergence of the flux function over each control volume is approximated by applying the divergence theorem to express the average in terms of averages of fluxes over the faces, which are then computed using some quadrature rule. The main advantage is that the resulting discretization satisfies a discrete form of the divergence theorem. This leads to a local conservation property holding for time-dependent problems and easily-checked solvability conditions for steady-state problems. Furthermore, this approach extends to a wide variety of grid systems: Cartesian, mapped, multiblock, and locally-refined structured grids, as well as unstructured grids. A limitation of these methods as developed to date is that they have typically been restricted to second-order accuracy [1–3]. The flux integrals are approximated using the midpoint rule, and the metric terms appearing in the quadrature computed using low-order geometric representations (*e.g.* unions of triangles).

In this paper, we present an approach for constructing finite-volume methods of any order of accuracy for control-volume discretizations of space defined as the image of a smooth mapping from a rectangular discretization of an abstract coordinate space. Our approach is based on two ideas. The first is that of using higher-order quadrature rules to compute the flux averages over faces that generalize the method described in [4] to the case of mapped grids. The second is a method for computing the averages of the metric terms on faces such that freestream preservation is automatically satisfied.

Freestream preservation is an important requirement for the discretization of conservation laws in mapped coordinates. This property ensures that a uniform flow is unaffected by the choice of mapping and discretization. As described in numerous works (*e.g.*, [1,5,6]), this goal is typically accomplished by the discrete enforcement of metric identities, which take the form of divergence-free conditions for products of the mapping Jacobian and gradients. Since cell faces are contractible (continuously deformable to a point), the Poincaré lemma guarantees that these products can be written as exterior derivatives. The form of these derivatives is not unique, however (see, *e.g.*, Section 4 of [6]), and the specific choice used for discretization is critical in achieving freestream preservation. In [5], it is observed that writing the derivatives in “conservative form” is sufficient to enable second-order central differencing to be applied in

---

the US Department of Energy under contract number DE-AC02-05CH11231.

the exact enforcement of the metric identities. This result was more recently extended in [7] to higher-order (second-, fourth- and sixth-order) compact, finite difference operators. The equivalence of the central difference scheme used in [5] with a second-order, finite-volume method was also used to obtain an early result for this class of methods. For the higher-order finite-volume discretizations presented here, we describe how to take further advantage of the ability to express mapping metric products as exterior derivatives to achieve freestream preservation.

The paper is organized as follows. A formalism for computing a fourth-order accurate average of a flux divergence on a control volume in physical space in terms of fourth-order accurate face averages on a Cartesian computational grid is developed in Section 2. In Section 3, we describe the application of the mapped grid finite-volume formalism to obtain a fourth-order accurate discretization of a self-adjoint elliptic equation. In Section 4, we describe the application of the formalism to obtain a fourth-order accurate discretization of a scalar, linear hyperbolic equation. The spatial discretization is combined with Runge-Kutta time discretization and the new high-order accurate limiter in [8] to obtain a method that is robust in the presence of discontinuities and under-resolved gradients.

## 2 High-Order Finite-Volume Methods

In the finite-volume approach, the spatial domain in  $\mathbb{R}^D$  is discretized as a union of rectangular control volumes that covers the spatial domain. For Cartesian grid finite-volume methods, a control volume  $V_{\mathbf{i}}$  takes the form

$$V_{\mathbf{i}} = \left[ i_1 - \frac{h}{2}, i_1 + \frac{h}{2} \right] \times \left[ i_2 - \frac{h}{2}, i_2 + \frac{h}{2} \right] \times \dots \times \left[ i_D - \frac{h}{2}, i_D + \frac{h}{2} \right], \quad (1)$$

where the multi-index  $\mathbf{i} \equiv (i_1, i_2, \dots, i_D) \in \mathbb{Z}^D$  is identified with the location of the control volume center and  $h$  is the grid spacing. A finite-volume method discretizes a partial differential equation by averaging that equation over control volumes and replacing the integrals that appear by quadratures. For right-hand sides that appear as the divergence of fluxes, the divergence theorem states that

$$\int_{V_{\mathbf{i}}} \nabla \cdot \mathbf{F} d\mathbf{x} = \sum_{\pm=+,-} \sum_{d=1}^D \pm \int_{A_d^{\pm}} F_d d\mathbf{A}, \quad (2)$$

where  $F_d$  is the  $d^{\text{th}}$  component of  $\mathbf{F}$  and the  $A_d^{\pm}$  are the high and low faces bounding  $V_{\mathbf{i}}$  with normals pointing the  $d^{\text{th}}$  coordinate direction. In this case, the finite-volume approach computes the average of the divergence of the fluxes

on the left-hand side of (2) with the sum of the integrals on the right-hand side, with the integrals approximated using quadratures. Such approximations are desirable because they lead to conserved quantities in the original PDE satisfying an analogous conservation law in the discretized system.

Most finite-volume methods use the midpoint rule to approximate the flux integrals in (2), leading to a second-order accurate method. We will develop higher-order methods (fourth-order or better) using the approach in [4]. The starting point for this approach is to replace the integrand in the right-hand side of (2) by a Taylor expansion about the center of the face:

$$\int_{A_d} F_d d\mathbf{A} = \sum_{0 \leq |\mathbf{r}| < R} \frac{1}{\mathbf{r}!} \nabla^{\mathbf{r}} F_d|_{x=x_0} \int_{A_d} (\mathbf{x} - \mathbf{x}_0)^{\mathbf{r}} dA_x + O(h^{R+D-1}), \quad (3)$$

$$\mathbf{r}! = r_1! \dots r_D! , \quad \mathbf{q}^{\mathbf{r}} = q_1^{r_1} \dots q_D^{r_D}.$$

For example, if we take  $R = 4$ , we obtain

$$\frac{1}{h^{D-1}} \int_{A_d} F_d d\mathbf{A} = F_d(\mathbf{x}_0) + \frac{h^2}{24} \sum_{d' \neq d} \frac{\partial^2 F_d}{\partial x_{d'}^2}(\mathbf{x}_0) + O(h^4). \quad (4)$$

If we replace the derivatives by finite-difference approximations of a suitable order that are smooth functions of their inputs, the resulting approximation of the average of the flux divergence over a cell is  $O(h^R)$ .

## 2.1 Mapped Grids

We can extend this formalism to the case of mapped grids. Assume that we have a smooth mapping  $\mathbf{X}$  from some abstract coordinate space, say, the unit cube, into physical space:

$$\mathbf{X} = \mathbf{X}(\boldsymbol{\xi}) , \quad \mathbf{X} : [0, 1]^D \rightarrow \mathbb{R}^D. \quad (5)$$

Given this mapping, the divergence of a vector field in physical space can be written in terms of derivatives in the mapping space, that is,

$$\nabla_{\mathbf{x}} \cdot \mathbf{F} = \frac{1}{J} \nabla_{\boldsymbol{\xi}} \cdot (\mathbf{N}^T \mathbf{F}), \quad (6)$$

$$J = \det(\nabla_{\boldsymbol{\xi}} \mathbf{X}) , \quad (\mathbf{N}^T)_{p,q} = \det((\nabla_{\boldsymbol{\xi}} \mathbf{X})(p|\mathbf{e}^q)),$$

where  $\mathbf{A}(p|\mathbf{v})$  denotes the matrix obtained by replacing the  $p^{\text{th}}$  row of the matrix  $\mathbf{A}$  by the vector  $\mathbf{v}$ , and  $\mathbf{e}^d$  denotes the unit vector in the  $d^{\text{th}}$  coordinate direction. The relationship (6) is a consequence of the chain rule, Cramer's rule and (for  $D > 2$ ) the equality of mixed partial derivatives.

If we define control volumes in physical space as the images  $\mathbf{X}(V_i)$  of the cubic control volumes  $V_i$  in the mapped Cartesian grid space, the relationship corresponding to (2) for mapped grids is given as follows:

$$\int_{\mathbf{X}(V_i)} \nabla_{\mathbf{x}} \cdot \mathbf{F} d\mathbf{x} = \int_{V_i} \nabla_{\boldsymbol{\xi}} \cdot (\mathbf{N}^T \mathbf{F}) d\boldsymbol{\xi} = \sum_{\pm=+,-} \sum_{d=1}^D \pm \int_{A_d^\pm} (\mathbf{N}^T \mathbf{F})_d d\mathbf{A}_\boldsymbol{\xi}. \quad (7)$$

To obtain a finite-volume method, the face integrals are replaced by quadratures, similar to what was done in (3). In the mapped-grid case, some care is required to obtain freestream preservation, that is, the property that the discrete divergence of a constant vector field is zero. To do that, we split each face integral into two pieces:

$$\int_{A_d} (\mathbf{N}^T \mathbf{F})_d d\mathbf{A}_\boldsymbol{\xi} = \left( \left( \int_{A_d} \mathbf{N}^T d\mathbf{A}_\boldsymbol{\xi} \right) \mathbf{F}(\mathbf{x}_d) \right)_d + \int_{A_d} (\mathbf{N}^T (\mathbf{F} - \mathbf{F}(\mathbf{x}_d)))_d d\mathbf{A}_\boldsymbol{\xi}, \quad (8)$$

where  $\mathbf{x}_d$  is the image under the map of the center of the face in coordinate space. It is routine to derive a version of the Taylor expansion in (3) to approximate the second integrand on the right-hand side of (8) so that, if  $\mathbf{F}$  is constant, the integral is identically zero. To obtain a fourth-order accurate discretization, we can use the following formulation

$$\begin{aligned} \int_{A_d} (\mathbf{N}^T \mathbf{F})_d d\mathbf{A}_\boldsymbol{\xi} &= \left( \left( \int_{A_d} \mathbf{N}^T d\mathbf{A}_\boldsymbol{\xi} \right) \cdot \left( \int_{A_d} \mathbf{F} d\mathbf{A}_\boldsymbol{\xi} \right) \right)_d \\ &\quad + \frac{h^2}{12} \int_{A_d} \sum_{d' \neq d} \left( \frac{\partial}{\partial \xi_{d'}} (\mathbf{N}^T) \cdot \frac{\partial}{\partial \xi_{d'}} (\mathbf{F}) \right)_d d\mathbf{A}_\boldsymbol{\xi} + O(h^4), \end{aligned} \quad (9)$$

as  $h \rightarrow 0$ . In either case, we only need to derive quadrature formulas for  $\int_{A_d} \mathbf{N}^T d\mathbf{A}_\boldsymbol{\xi}$  so that the discrete divergence of a constant vector field given by (8) or (9) is zero.

The existence of such quadratures is a consequence of Stokes' theorem and the Poincaré lemma. The rows of the matrix  $\mathbf{N}$ , denoted by  $N^s$ ,  $s = 1, \dots, D$  are divergence-free. This can be seen by a direct calculation, or inferred indirectly from applying (7) to constant vector fields. Then by the Poincaré lemma [9], there exist functions  $\mathcal{N}_{d,d'}^s$ ,  $d \neq d'$  such that

$$N_d^s = \sum_{d' \neq d} \frac{\partial \mathcal{N}_{d,d'}^s}{\partial \xi_{d'}}, \quad \mathcal{N}_{d,d'}^s = -\mathcal{N}_{d',d}^s. \quad (10)$$

Thus we have

$$\int_{A_d} N_d^s d\mathbf{A}_\boldsymbol{\xi} = \sum_{\pm=+,-} \sum_{d' \neq d} \pm \int_{E_{d,d'}^\pm} \mathcal{N}_{d,d'}^s d\mathbf{E}_\boldsymbol{\xi}, \quad (11)$$

where  $E_{d,d'}^\pm$  are the (hyper)edges on the low and high sides of  $A_d$  in the  $d'$  direction. For each edge, the same integrals over the edge appear for the integral over each face adjacent to that edge, modulo signs. If we approximate the integrals over edges with the same quadrature formulas wherever they appear, then the freestream property

$$\sum_{d=1}^D \sum_{\pm=+,-} \pm \int_{A_d^\pm} N_d^s d\mathbf{A}_\xi = 0 \quad (12)$$

is satisfied. Furthermore, the quadrature formulas for the edge integrals can otherwise be chosen arbitrarily; in particular, they can be chosen so that (11) approximates the integral of  $N_d^s$  over the face to any order of accuracy. We note that this is a generalization to arbitrary dimensions and arbitrary orders of accuracy of standard methods to discretize electromagnetic fields so that discrete analogues of the various vector identities are satisfied identically [10].

Given  $N_d^s$ ,  $d = 1, \dots, D$ , the family of functions  $\mathcal{N}_{d,d'}^s$ ,  $d' \neq d$ , satisfying (10) is not unique. A particularly simple choice that is a local function of  $\mathbf{X}$  and  $\nabla_\xi \mathbf{X}$  is given by

$$\mathcal{N}_{d,d'}^s = \frac{1}{D-1} \det \left( (\nabla_\xi \mathbf{X}) (\mathbf{X}|d')(s|\mathbf{e}^d) \right), \quad (13)$$

where  $\mathbf{A}(\mathbf{v}|p)$  denotes the matrix obtained by replacing the  $p^{\text{th}}$  column of the matrix  $\mathbf{A}$  with  $\mathbf{v}$ . We note that the expression for  $\mathcal{N}_{d,d}^s$  given above only involves derivatives of  $\mathbf{X}$  in directions tangent to  $E_{d,d}$ . For convenience, the  $\mathcal{N}_{d,d}^s$  for the special case of  $D = 3$  are given as follows.

$$\begin{aligned} \mathcal{N}_{21}^1 &= \frac{1}{2} \left( X_3 \frac{\partial X_2}{\partial \xi_3} - X_2 \frac{\partial X_3}{\partial \xi_3} \right) & \mathcal{N}_{21}^2 &= \frac{1}{2} \left( -X_3 \frac{\partial X_1}{\partial \xi_3} + X_1 \frac{\partial X_3}{\partial \xi_3} \right) \\ \mathcal{N}_{21}^3 &= \frac{1}{2} \left( X_2 \frac{\partial X_1}{\partial \xi_3} - X_1 \frac{\partial X_2}{\partial \xi_3} \right) & \mathcal{N}_{31}^1 &= \frac{1}{2} \left( -X_3 \frac{\partial X_2}{\partial \xi_2} + X_2 \frac{\partial X_3}{\partial \xi_2} \right) \\ \mathcal{N}_{31}^2 &= \frac{1}{2} \left( X_3 \frac{\partial X_1}{\partial \xi_2} - X_1 \frac{\partial X_3}{\partial \xi_2} \right) & \mathcal{N}_{31}^3 &= \frac{1}{2} \left( -X_2 \frac{\partial X_1}{\partial \xi_2} + X_1 \frac{\partial X_2}{\partial \xi_2} \right) \\ \mathcal{N}_{32}^1 &= \frac{1}{2} \left( X_3 \frac{\partial X_2}{\partial \xi_1} - X_2 \frac{\partial X_3}{\partial \xi_1} \right) & \mathcal{N}_{32}^2 &= \frac{1}{2} \left( -X_3 \frac{\partial X_1}{\partial \xi_1} + X_1 \frac{\partial X_3}{\partial \xi_1} \right) \\ \mathcal{N}_{32}^3 &= \frac{1}{2} \left( X_2 \frac{\partial X_1}{\partial \xi_1} - X_1 \frac{\partial X_2}{\partial \xi_1} \right). \end{aligned} \quad (14)$$

The remaining  $\mathcal{N}$ 's are given by the antisymmetry condition  $\mathcal{N}_{d,d'}^s = -\mathcal{N}_{d',d}^s$ .

The proof that (13) satisfies (10) is a straightforward calculation. By Leibnitz'

rule applied to determinants, we have

$$\begin{aligned}
& \sum_{d' \neq d} \frac{\partial}{\partial \xi_{d'}} \left( \det \left( (\nabla_{\boldsymbol{\xi}} \mathbf{X}) (\mathbf{X}|d')(s|\mathbf{e}^d) \right) \right) \\
&= \sum_{d' \neq d} \det \left( (\nabla_{\boldsymbol{\xi}} \mathbf{X}) \left( \frac{\partial \mathbf{X}}{\partial \xi_{d'}} |d' \right) (s|\mathbf{e}^d) \right) \\
&+ \sum_{d' \neq d} \sum_{d'' \neq d, d'} \det \left( (\nabla_{\boldsymbol{\xi}} \mathbf{X}) (\mathbf{X}|d') \left( \frac{\partial^2 \mathbf{X}}{\partial \xi_{d'} \partial \xi_{d''}} |d'' \right) (s|\mathbf{e}^d) \right).
\end{aligned} \tag{15}$$

Each summand in the first (single) sum is just  $N_d^s$ , so it suffices to show that the second (double) sum vanishes. However, for a given  $d_1, d_2, d_1 \neq d_2$ , summands in the double sum involving the mixed second partial  $\frac{\partial^2 \mathbf{X}}{\partial \xi_{d_1} \partial \xi_{d_2}}$  appear exactly twice, differing from one another only by the exchange of the  $d_1$  and  $d_2$  columns. By the antisymmetry of the determinant under column exchanges, the two summands cancel, and hence the entire second sum vanishes. Finally, we need to show the antisymmetry condition  $\mathcal{N}_{d,d'}^s = -\mathcal{N}_{d',d}^s$ . The following is a consequence of linearity of the determinant as a function of the  $d'$  column, plus the identity  $\det(\mathbf{A}(\mathbf{e}^p|q)) = \det(\mathbf{A}(q|\mathbf{e}^p))$ :

$$\det \left( (\nabla_{\boldsymbol{\xi}} \mathbf{X}) (\mathbf{X}|d')(s|\mathbf{e}^d) \right) = \sum_{s' \neq s} X_{s'} \det \left( (\nabla_{\boldsymbol{\xi}} \mathbf{X}) (s|\mathbf{e}^d)(s'|\mathbf{e}^{d'}) \right). \tag{16}$$

The right-hand side of (16) is manifestly antisymmetric in  $d, d'$ .

## 2.2 Fourth-order mapped-grid finite-volume discretization

Following these ideas, we can specify the information required for a fourth-order accurate finite-volume discretization. Using a Taylor series, the integrals on the cell faces  $A_d^\pm$  can be approximated using the following formula for the average of a product in terms of fourth-order accurate averages of each factor:

$$\begin{aligned}
\langle fg \rangle_{\mathbf{i} + \frac{1}{2} \mathbf{e}^d} &= \\
& \langle f \rangle_{\mathbf{i} + \frac{1}{2} \mathbf{e}^d} \langle g \rangle_{\mathbf{i} + \frac{1}{2} \mathbf{e}^d} + \frac{h^2}{12} \mathbf{G}_0^{\perp, d} \left( \langle f \rangle_{\mathbf{i} + \frac{1}{2} \mathbf{e}^d} \right) \cdot \mathbf{G}_0^{\perp, d} \left( \langle g \rangle_{\mathbf{i} + \frac{1}{2} \mathbf{e}^d} \right) + O(h^4).
\end{aligned} \tag{17}$$

Here,  $\mathbf{G}_0^{\perp, d}$  is the second-order accurate central difference approximation to the components of the gradient operator orthogonal to the  $d$ -th direction:  $\mathbf{G}_0^{\perp, d} \approx \nabla_{\boldsymbol{\xi}} - \mathbf{e}^d \frac{\partial}{\partial \xi_d}$ , and the operator  $\langle \cdot \rangle_{\mathbf{i} + \frac{1}{2} \mathbf{e}^d}$  denotes a fourth-order accurate average over the face centered at  $\mathbf{i} + \frac{1}{2} \mathbf{e}^d$ :

$$\langle q \rangle_{\mathbf{i} + \frac{1}{2} \mathbf{e}^d} = \frac{1}{h^{D-1}} \int_{A_d} q(\boldsymbol{\xi}) d\mathbf{A}_{\boldsymbol{\xi}} + O(h^4). \tag{18}$$

Alternative expressions to (17) are obtained by replacing the averages  $\langle f \rangle_{\mathbf{i}+\frac{1}{2}\mathbf{e}^d}$  and/or  $\langle g \rangle_{\mathbf{i}+\frac{1}{2}\mathbf{e}^d}$  used in the transverse gradients  $\mathbf{G}_0^{\perp,d}$  by the corresponding face-centered pointwise values  $f_{\mathbf{i}+\frac{1}{2}\mathbf{e}^d}$  and/or  $g_{\mathbf{i}+\frac{1}{2}\mathbf{e}^d}$ , respectively.

We then approximate the divergence of a flux by

$$\int_{\mathbf{X}(V_i)} \nabla_{\mathbf{x}} \cdot \mathbf{F} d\mathbf{x} \approx h^{D-1} \sum_{d=1}^D \sum_{\pm=+,-} \pm F_{\mathbf{i} \pm \frac{1}{2} \mathbf{e}^d}^d, \quad (19)$$

where

$$F_{\mathbf{i} \pm \frac{1}{2} \mathbf{e}^d}^d = \sum_{s=1}^D \langle N_d^s \rangle_{\mathbf{i} \pm \frac{1}{2} \mathbf{e}^d} \langle F^s \rangle_{\mathbf{i} \pm \frac{1}{2} \mathbf{e}^d} + \frac{h^2}{12} \sum_{s=1}^D \left( \mathbf{G}_0^{\perp,d}(\langle N_d^s \rangle_{\mathbf{i} \pm \frac{1}{2} \mathbf{e}^d}) \cdot \left( \mathbf{G}_0^{\perp,d}(\langle F^s \rangle_{\mathbf{i} \pm \frac{1}{2} \mathbf{e}^d}) \right) \right). \quad (20)$$

The column vectors  $\{\langle N_d^s \rangle_{\mathbf{i} \pm \frac{1}{2} \mathbf{e}^d}, s = 1, \dots, D\}$  are computed on each face using (11) and (13), with fourth-order accurate quadratures replacing the integrals in (11). The fourth-order average of  $\mathbf{F}$  can be computed using (4).

We can apply this approach to compute a fourth-order accurate approximation to the cell volumes by taking  $\mathbf{F}(\mathbf{x}) = \mathbf{x}$ . In that case,

$$\int_{\mathbf{X}(V_i)} \nabla_{\mathbf{x}} \cdot \mathbf{F} d\mathbf{x} = D \times \text{Volume}(\mathbf{X}(V_i)),$$

and the volume of the cell can be written as the discrete divergence of fluxes. Such a flux form is convenient for maintaining conservation and freestream preservation for adaptive mesh refinement on mapped grids [11].

### 3 Application to Elliptic Equations

In this section, we apply the mapped grid, finite-volume formalism described above to obtain a fourth-order accurate finite-volume discretization of a self-adjoint equation

$$\nabla \cdot \mathbf{F}(\mathbf{x}) = \rho(\mathbf{x}), \quad \mathbf{x} \in \Omega \subset \mathbb{R}^2, \quad (21)$$

where

$$\mathbf{F}(\mathbf{x}) \equiv \mathbf{D}(\mathbf{x}) \nabla \Phi(\mathbf{x}), \quad (22)$$

and the matrix coefficient  $\mathbf{D}$  is such that the second-order differential operator in (21)-(22) is elliptic. Assuming a mapping (5) of the physical domain  $\Omega$  to a computational domain, we have in the latter using (6)

$$\mathbf{F} = \mathbf{D} \nabla_{\mathbf{x}} \xi \nabla_{\xi} \Phi \equiv J^{-1} \mathbf{D} \mathbf{N} \nabla_{\xi} \Phi. \quad (23)$$

Following (19) and (20), we therefore obtain

$$\int_{\mathbf{x}(V_i)} \nabla_{\mathbf{x}} \cdot \mathbf{F} d\mathbf{x} = h^2 \sum_{d=1}^3 \sum_{\pm=+,-} \pm F^d_{\mathbf{i} \pm \frac{1}{2} \mathbf{e}^d} + O(h^4), \quad (24)$$

where, using face-centered pointwise values of  $\mathbf{F}$  in the transverse gradients,

$$\begin{aligned} F^d_{\mathbf{i} + \frac{1}{2} \mathbf{e}^d} &\equiv \langle \mathbf{F}^d \rangle_{\mathbf{i} + \frac{1}{2} \mathbf{e}^d} = \sum_{d'=1}^3 \left\langle \widetilde{\mathbf{D}}_{dd'} \frac{\partial \Phi}{\partial \xi_{d'}} \right\rangle_{\mathbf{i} + \frac{1}{2} \mathbf{e}^d} \\ &= \sum_{d'=1}^3 \left[ \left\langle \widetilde{\mathbf{D}}_{dd'} \right\rangle_{\mathbf{i} + \frac{1}{2} \mathbf{e}^d} \left\langle \frac{\partial \Phi}{\partial \xi_{d'}} \right\rangle_{\mathbf{i} + \frac{1}{2} \mathbf{e}^d} \right. \\ &\quad \left. + \frac{h^2}{12} \mathbf{G}_0^{\perp, d} \left( \left\langle \widetilde{\mathbf{D}}_{dd'} \right\rangle \right)_{\mathbf{i} + \frac{1}{2} \mathbf{e}^d} \cdot \mathbf{G}_0^{\perp, d} \left( \frac{\partial \Phi}{\partial \xi_{d'}} \right)_{\mathbf{i} + \frac{1}{2} \mathbf{e}^d} \right] \end{aligned} \quad (25)$$

where

$$\widetilde{\mathbf{D}} \equiv \left( \widetilde{\mathbf{D}}_{dd'} \right) \equiv J^{-1} \mathbf{N}^T \mathbf{D} \mathbf{N}. \quad (26)$$

Face averages  $\langle \widetilde{\mathbf{D}}_{dd'} \rangle$  can be computed to fourth order in terms of face averages of the entries of the factor matrices  $\mathbf{N}^T$ ,  $\mathbf{D}$  and  $J^{-1} \mathbf{N}$  using the product formula (17). Computing the second-order accurate transverse gradients

$$\mathbf{G}_0^{\perp, d} \left( \left\langle \widetilde{\mathbf{D}}_{dd'} \right\rangle \right)_{\mathbf{i} + \frac{1}{2} \mathbf{e}^d} \equiv \frac{1}{h} \left( \left\langle \widetilde{\mathbf{D}}_{dd'} \right\rangle_{\mathbf{i} + \frac{1}{2} \mathbf{e}^d + \mathbf{e}^d} - \left\langle \widetilde{\mathbf{D}}_{dd'} \right\rangle_{\mathbf{i} + \frac{1}{2} \mathbf{e}^d - \mathbf{e}^d} \right), \quad (27)$$

it then remains to specify the discretization of the averages  $\langle \partial \Phi / \partial \xi_{d'} \rangle_{\mathbf{i} + \frac{1}{2} \mathbf{e}^d}$  and transverse gradient  $\mathbf{G}_0^{\perp, d} (\partial \Phi / \partial \xi_{d'})_{\mathbf{i} + \frac{1}{2} \mathbf{e}^d}$ .

### 3.1 Discretization of $\langle \partial \Phi / \partial \xi_{d'} \rangle_{\mathbf{i} + \frac{1}{2} \mathbf{e}^d}$ and $\mathbf{G}_0^{\perp, d} (\partial \Phi / \partial \xi_{d'})_{\mathbf{i} + \frac{1}{2} \mathbf{e}^d}$

First consider the case where  $d' = d$ . We have

$$\left\langle \frac{\partial \Phi}{\partial \xi_d} \right\rangle_{\mathbf{i} + \frac{1}{2} \mathbf{e}^d} = \left( \frac{\partial \Phi}{\partial \xi_d} + \frac{h^2}{24} \Delta^{\perp, d} \frac{\partial \Phi}{\partial \xi_d} \right)_{\mathbf{i} + \frac{1}{2} \mathbf{e}^d} + O(h^4), \quad (28)$$

where  $\Delta^{\perp, d}$  is the Laplacian in the directions transverse to the  $d$ -th direction. Defining

$$\beta_{\mathbf{i} + \frac{1}{2} \mathbf{e}^d} \equiv \frac{1}{24} [27 (\Phi_{\mathbf{i} + \mathbf{e}^d} - \Phi_{\mathbf{i}}) - (\Phi_{\mathbf{i} + 2\mathbf{e}^d} - \Phi_{\mathbf{i} - \mathbf{e}^d})], \quad (29)$$

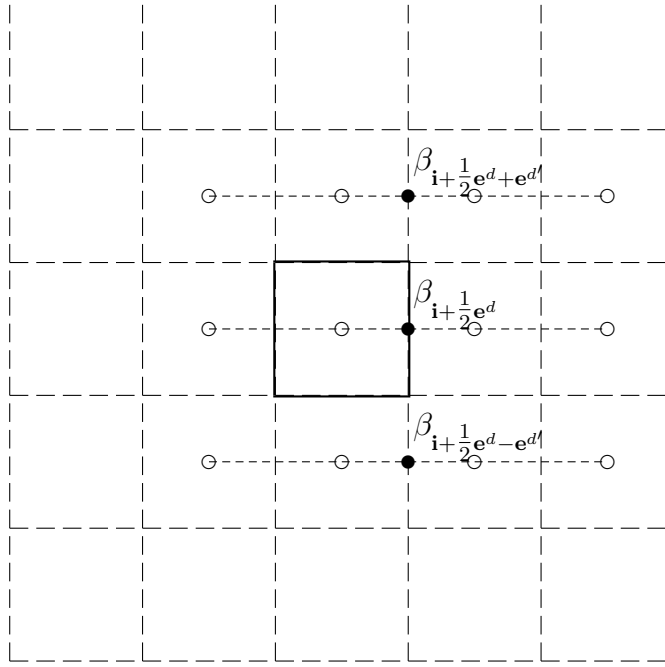


Fig. 1. Stencil for  $\langle \partial\Phi/\partial\xi_d \rangle_{i+\frac{1}{2}\mathbf{e}^d}$ . The values of  $\Phi$  at the cell centers marked by the open circles determine the  $\beta$  values given by (29) at the cell faces marked by the solid circles.

where the  $\Phi_i$  denote pointwise values of  $\Phi$  at cell centers, we have

$$\frac{\partial\Phi}{\partial\xi_d}\Big|_{i+\frac{1}{2}\mathbf{e}^d} = \frac{\beta_{i+\frac{1}{2}\mathbf{e}^d}}{h} + O(h^4), \quad (30)$$

$$\Delta^{\perp,d}\frac{\partial\Phi}{\partial\xi_d}\Big|_{i+\frac{1}{2}\mathbf{e}^d} = \frac{1}{h^3} \sum_{d' \neq d} \left( \beta_{i+\frac{1}{2}\mathbf{e}^d+\mathbf{e}^{d'}} + \beta_{i+\frac{1}{2}\mathbf{e}^d-\mathbf{e}^{d'}} - 2\beta_{i+\frac{1}{2}\mathbf{e}^d} \right) + O(h^2). \quad (31)$$

Furthermore, we set

$$\mathbf{G}_0^{\perp,d} \left( \frac{\partial\Phi}{\partial\xi_d} \right)_{i+\frac{1}{2}\mathbf{e}^d} \equiv \frac{1}{h^2} \left( \beta_{i+\frac{1}{2}\mathbf{e}^d+\mathbf{e}^{d'}} - \beta_{i+\frac{1}{2}\mathbf{e}^d-\mathbf{e}^{d'}} \right). \quad (32)$$

Next, for  $d' \neq d$ , we have

$$\left\langle \frac{\partial\Phi}{\partial\xi_{d'}} \right\rangle_{i+\frac{1}{2}\mathbf{e}^d} = \left( \frac{\partial\Phi}{\partial\xi_{d'}} + \frac{h^2}{24} \frac{\partial^3\Phi}{\partial\xi_{d'}^3} \right)_{i+\frac{1}{2}\mathbf{e}^d} + O(h^4). \quad (33)$$

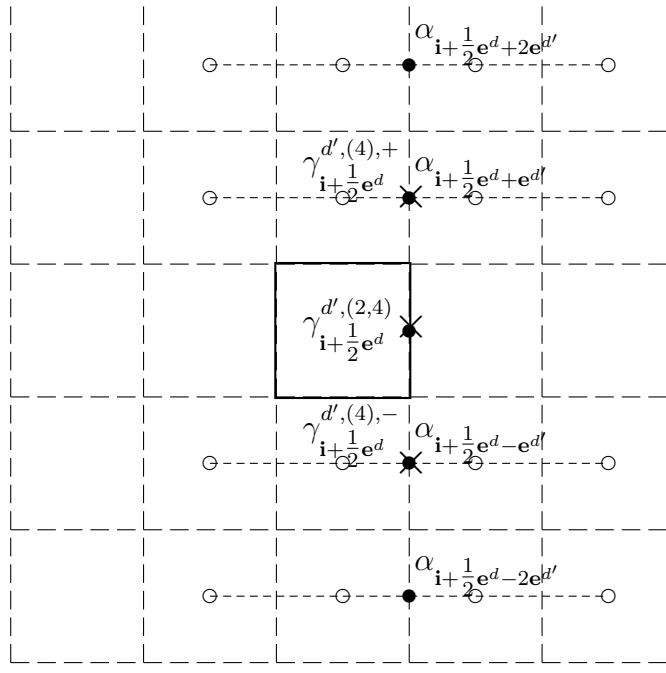


Fig. 2. Stencil for  $\langle \partial\Phi/\partial\xi_{d'} \rangle_{i+\frac{1}{2}\mathbf{e}^d}$  with  $d' \neq d$ . The values of  $\Phi$  at the cell centers marked by the  $\circ$  symbols determine the  $\alpha$  values at the  $\bullet$  symbols via (34), which in turn determine the  $\gamma$  values at the  $\times$  symbols defined by (37)–(39).

Letting

$$\alpha_{i+\frac{1}{2}\mathbf{e}^d} \equiv \frac{1}{16} [9(\Phi_{i+\mathbf{e}^d} + \Phi_{\mathbf{i}}) - (\Phi_{i+2\mathbf{e}^d} + \Phi_{i-\mathbf{e}^d})], \quad (34)$$

$$\gamma_{i+\frac{1}{2}\mathbf{e}^d}^{d',(4)} \equiv \frac{1}{12} \left[ 8(\alpha_{i+\frac{1}{2}\mathbf{e}^d + \mathbf{e}^{d'}} - \alpha_{i+\frac{1}{2}\mathbf{e}^d - \mathbf{e}^{d'}}) - (\alpha_{i+\frac{1}{2}\mathbf{e}^d + 2\mathbf{e}^{d'}} - \alpha_{i+\frac{1}{2}\mathbf{e}^d - 2\mathbf{e}^{d'}}) \right], \quad (35)$$

$$\gamma_{i+\frac{1}{2}\mathbf{e}^d}^{d',(2)} \equiv \frac{1}{2} \left[ -2(\alpha_{i+\frac{1}{2}\mathbf{e}^d + \mathbf{e}^{d'}} - \alpha_{i+\frac{1}{2}\mathbf{e}^d - \mathbf{e}^{d'}}) + (\alpha_{i+\frac{1}{2}\mathbf{e}^d + 2\mathbf{e}^{d'}} - \alpha_{i+\frac{1}{2}\mathbf{e}^d - 2\mathbf{e}^{d'}}) \right], \quad (36)$$

we have

$$\frac{\partial\Phi}{\partial\xi_{d'}} \Big|_{i+\frac{1}{2}\mathbf{e}^d} = \frac{\gamma_{i+\frac{1}{2}\mathbf{e}^d}^{d',(4)}}{h} + O(h^4), \quad (37)$$

$$\frac{\partial^3\Phi}{\partial\xi_{d'}^3} \Big|_{i+\frac{1}{2}\mathbf{e}^d} = \frac{\gamma_{i+\frac{1}{2}\mathbf{e}^d}^{d',(2)}}{h^3} + O(h^2). \quad (38)$$

Defining

$$\gamma_{i+\frac{1}{2}\mathbf{e}^d}^{d',(4),\pm} \equiv \pm \frac{1}{12} \left[ 3\alpha_{i+\frac{1}{2}\mathbf{e}^d \pm 2\mathbf{e}^{d'}} + 10\alpha_{i+\frac{1}{2}\mathbf{e}^d \pm \mathbf{e}^{d'}} - 18\alpha_{i+\frac{1}{2}\mathbf{e}^d} + 6\alpha_{i+\frac{1}{2}\mathbf{e}^d \mp \mathbf{e}^{d'}} - \alpha_{i+\frac{1}{2}\mathbf{e}^d \mp 2\mathbf{e}^{d'}} \right], \quad (39)$$

we furthermore set

$$\mathbf{G}_0^{\perp,d} \left( \frac{\partial \Phi}{\partial \xi_{d'}} \right)_{\mathbf{i} + \frac{1}{2} \mathbf{e}^d} \equiv \frac{1}{h^2} \left( \gamma_{\mathbf{i} + \frac{1}{2} \mathbf{e}^d}^{d',(4),+} - \gamma_{\mathbf{i} + \frac{1}{2} \mathbf{e}^d}^{d',(4),-} \right). \quad (40)$$

The stencil entries given by (39) yield fourth-order accurate first derivatives in the  $d'$  direction at the face centers  $\mathbf{i} + \frac{1}{2} \mathbf{e}^d \pm \mathbf{e}^{d'}$ . We employ these non-centered formulas to ensure that the resulting stencil is confined to block of cells at most 5 cells wide centered on the cell in which the flux divergence average is being computed.

### 3.2 Boundary conditions

For boundaries upon which a Dirichlet boundary condition is posed, the face averages  $\langle \partial \Phi / \partial \xi_{d'} \rangle_{\mathbf{i} + \frac{1}{2} \mathbf{e}^d}$  used in (25) on faces contained in such boundaries can be computed using modified discretizations that incorporate the prescribed boundary values. Suppose that the cell face with center at  $\mathbf{i} + \frac{1}{2} \mathbf{e}^d$  is one such face, such as the face centered on the point labeled A in Figure 3. The averages  $\langle \partial \Phi / \partial \xi_{d'} \rangle_{\mathbf{i} + \frac{1}{2} \mathbf{e}^d}$  for the transverse coordinates  $d' \neq d$  can presumably be computed directly from prescribed Dirichlet data to fourth-order accuracy. For the normal direction, the stencil describing  $\langle \partial \Phi / \partial \xi_d \rangle_{\mathbf{i} + \frac{1}{2} \mathbf{e}^d}$  can be modified by replacing the definition (29) by

$$\beta_{\mathbf{i} + \frac{1}{2} \mathbf{e}^d}^{(4)} \equiv \frac{1}{840} \left( 2816 \Phi_{\mathbf{i} + \frac{1}{2} \mathbf{e}^d} - 3675 \Phi_{\mathbf{i}} \right. \\ \left. + 1225 \Phi_{\mathbf{i} - \mathbf{e}^d} - 441 \Phi_{\mathbf{i} - 2\mathbf{e}^d} + 75 \Phi_{\mathbf{i} - 3\mathbf{e}^d} \right), \quad (41)$$

where  $\Phi_{\mathbf{i} + \frac{1}{2} \mathbf{e}^d}$  is the prescribed boundary value at the center of the cell face. Although this formula yields a fourth order accurate approximation of the normal derivative, it results in a stencil extending beyond the 5-cell-wide block centered about the cell upon which the discrete divergence is being computed. To avoid using a larger stencil at the boundary than in the interior, we take advantage of the opportunity to reduce the discretization order at the boundary while still maintaining fourth-order accuracy overall due to elliptic regularity. In particular, instead of (41) we define

$$\beta_{\mathbf{i} + \frac{1}{2} \mathbf{e}^d}^{(4)} \equiv \frac{1}{60} \left( 184 \Phi_{\mathbf{i} + \frac{1}{2} \mathbf{e}^d} - 225 \Phi_{\mathbf{i}} + 50 \Phi_{\mathbf{i} - \mathbf{e}^d} - 9 \Phi_{\mathbf{i} - 2\mathbf{e}^d} \right). \quad (42)$$

The same issue affects the normal and transverse derivatives on interior faces parallel to the boundary exactly one cell away, such as the face centered on the point labeled B in Figure 3, *i.e.*, the use of a non-centered fourth-order

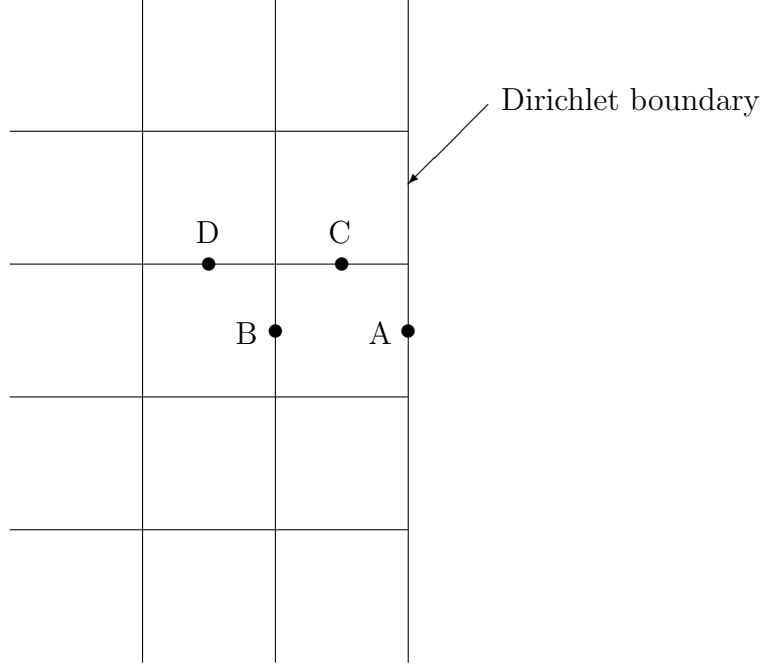


Fig. 3. Locations at or near a Dirichlet boundary requiring stencil modifications (see text).

discretization leads to a stencil that is not contained in a  $5 \times 5$  block. However, we may use the same interpolating cubic polynomial used in finding (42) to obtain

$$\beta_{\mathbf{i}+\frac{1}{2}\mathbf{e}^d}^{(4)} \equiv \frac{1}{60} \left( -8\Phi_{\mathbf{i}+\frac{1}{2}\mathbf{e}^d} + 75\Phi_{\mathbf{i}} - 70\Phi_{\mathbf{i}-\mathbf{e}^d} + 3\Phi_{\mathbf{i}-2\mathbf{e}^d} \right). \quad (43)$$

Similarly, (34) is replaced by

$$\alpha_{\mathbf{i}+\frac{1}{2}\mathbf{e}^d} \equiv \frac{1}{20} \left( -4\Phi_{\mathbf{i}+\frac{1}{2}\mathbf{e}^d} + 15\Phi_{\mathbf{i}} + 10\Phi_{\mathbf{i}-\mathbf{e}^d} - \Phi_{\mathbf{i}-2\mathbf{e}^d} \right). \quad (44)$$

Next, consider cell faces adjacent and normal to a Dirichlet boundary, such as the face centered on the point labeled C in Figure 3. For the calculation of the average of the normal derivative ( $d = d'$ ), the calculation of the transverse Laplacian (31) using centered differences can be shifted one cell away from the boundary with no loss of the required second-order accuracy. A non-centered, second-order accurate formula replaces (32):

$$\mathbf{G}_0^{\perp,d} \left( \frac{\partial \Phi}{\partial \xi_d} \right)_{\mathbf{i}+\frac{1}{2}\mathbf{e}^d} \equiv \frac{1}{2h^2} \left( 3\beta_{\mathbf{i}+\frac{1}{2}\mathbf{e}^d} - 4\beta_{\mathbf{i}+\frac{1}{2}\mathbf{e}^d-\mathbf{e}^{d'}} + \beta_{\mathbf{i}+\frac{1}{2}\mathbf{e}^d-2\mathbf{e}^{d'}} \right). \quad (45)$$

For the average of the transverse derivative ( $d \neq d'$ ), we replace (35) and (36)

by

$$\gamma_{\mathbf{i}+\frac{1}{2}\mathbf{e}^d}^{d',(4)} \equiv \frac{1}{30} \left[ 32\Phi_{\mathbf{i}+\frac{1}{2}\mathbf{e}^d+\frac{1}{2}\mathbf{e}^{d'}} - 15\alpha_{\mathbf{i}+\frac{1}{2}\mathbf{e}^d} - 20\alpha_{\mathbf{i}+\frac{1}{2}\mathbf{e}^d-\mathbf{e}^{d'}} + 3\alpha_{\mathbf{i}+\frac{1}{2}\mathbf{e}^d-2\mathbf{e}^{d'}} \right], \quad (46)$$

$$\gamma_{\mathbf{i}+\frac{1}{2}\mathbf{e}^d}^{d',(2)} \equiv \frac{1}{5} \left[ 16\Phi_{\mathbf{i}+\frac{1}{2}\mathbf{e}^d+\frac{1}{2}\mathbf{e}^{d'}} - 30\alpha_{\mathbf{i}+\frac{1}{2}\mathbf{e}^d} + 20\alpha_{\mathbf{i}+\frac{1}{2}\mathbf{e}^d-\mathbf{e}^{d'}} - 6\alpha_{\mathbf{i}+\frac{1}{2}\mathbf{e}^d-2\mathbf{e}^{d'}} \right], \quad (47)$$

where  $\Phi_{\mathbf{i}+\frac{1}{2}\mathbf{e}^d+\frac{1}{2}\mathbf{e}^{d'}}$  is the prescribed boundary value. This yields a third-order accurate first derivative and first-order accurate third derivative, respectively. We furthermore use for the transverse gradients

$$\mathbf{G}_0^{\perp,d} \left( \frac{\partial \Phi}{\partial \xi^{d'}} \right)_{\mathbf{i}+\frac{1}{2}\mathbf{e}^d} \equiv \frac{1}{5h^2} \left[ 16\Phi_{\mathbf{i}+\frac{1}{2}\mathbf{e}^d+\frac{1}{2}\mathbf{e}^{d'}} - 25\alpha_{\mathbf{i}+\frac{1}{2}\mathbf{e}^d} + 10\alpha_{\mathbf{i}+\frac{1}{2}\mathbf{e}^d-\mathbf{e}^{d'}} - \alpha_{\mathbf{i}+\frac{1}{2}\mathbf{e}^d-2\mathbf{e}^{d'}} \right]. \quad (48)$$

On cell faces normal to a Dirichlet boundary, the transverse gradients of the coefficient averages are obtained by replacing the centered formula in (27) by the second-order non-centered formula

$$\begin{aligned} & \mathbf{G}_0^{\perp,d} \left( \langle \widetilde{\mathbf{D}}_{dd'} \rangle \right)_{\mathbf{i}+\frac{1}{2}\mathbf{e}^d} \\ & \equiv \frac{1}{2h} \left( 3 \langle \widetilde{\mathbf{D}}_{dd'} \rangle_{\mathbf{i}+\frac{1}{2}\mathbf{e}^d} - 4 \langle \widetilde{\mathbf{D}}_{dd'} \rangle_{\mathbf{i}+\frac{1}{2}\mathbf{e}^d-\mathbf{e}^{d'}} + \langle \widetilde{\mathbf{D}}_{dd'} \rangle_{\mathbf{i}+\frac{1}{2}\mathbf{e}^d-2\mathbf{e}^{d'}} \right). \end{aligned} \quad (49)$$

Finally, consider cell faces normal to a Dirichlet boundary and one cell away, such as the face centered on the point labeled D in Figure 3. The average of the normal derivatives ( $d = d'$ ) is computed in the same manner as for the interior cells. For the average of the transverse derivative ( $d \neq d'$ ), we replace (35) and (36) by

$$\begin{aligned} \gamma_{\mathbf{i}+\frac{1}{2}\mathbf{e}^d}^{d',(4)} & \equiv \frac{1}{210} \left[ -64\Phi_{\mathbf{i}+\frac{1}{2}\mathbf{e}^d+\frac{1}{2}\mathbf{e}^{d'}} + 210\alpha_{\mathbf{i}+\frac{1}{2}\mathbf{e}^d+\mathbf{e}^{d'}} \right. \\ & \quad \left. - 35\alpha_{\mathbf{i}+\frac{1}{2}\mathbf{e}^d} - 126\alpha_{\mathbf{i}+\frac{1}{2}\mathbf{e}^d-\mathbf{e}^{d'}} + 15\alpha_{\mathbf{i}+\frac{1}{2}\mathbf{e}^d-2\mathbf{e}^{d'}} \right], \end{aligned} \quad (50)$$

$$\begin{aligned} \gamma_{\mathbf{i}+\frac{1}{2}\mathbf{e}^d}^{d',(2)} & \equiv \frac{1}{35} \left[ 64\Phi_{\mathbf{i}+\frac{1}{2}\mathbf{e}^d+\frac{1}{2}\mathbf{e}^{d'}} - 105\alpha_{\mathbf{i}+\frac{1}{2}\mathbf{e}^d+\mathbf{e}^{d'}} \right. \\ & \quad \left. + 35\alpha_{\mathbf{i}+\frac{1}{2}\mathbf{e}^d} + 21\alpha_{\mathbf{i}+\frac{1}{2}\mathbf{e}^d-\mathbf{e}^{d'}} - 15\alpha_{\mathbf{i}+\frac{1}{2}\mathbf{e}^d-2\mathbf{e}^{d'}} \right], \end{aligned} \quad (51)$$

where again  $\Phi_{\mathbf{i}+\frac{1}{2}\mathbf{e}^d+\frac{1}{2}\mathbf{e}^{d'}}$  is the prescribed boundary value. This yields a fourth-order accurate first derivative and second-order accurate third derivative, respectively. We furthermore use for the transverse gradients the second-order

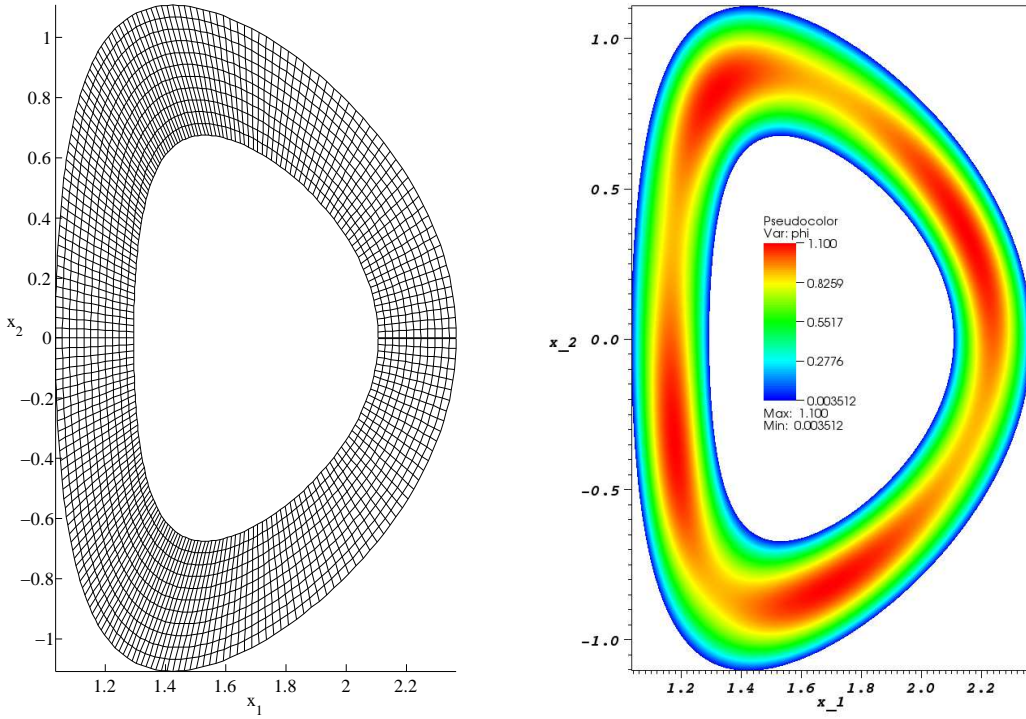


Fig. 4. Test problem geometry  $\Omega$  (left) and solution computed with  $N = 512$  (right).

formula

$$\mathbf{G}_0^{\perp,d} \left( \frac{\partial \Phi}{\partial \xi_{d'}} \right)_{\mathbf{i} + \frac{1}{2} \mathbf{e}^d} = \frac{1}{105h^2} \left[ 32\Phi_{\mathbf{i} + \frac{1}{2} \mathbf{e}^d + \frac{1}{2} \mathbf{e}^{d'}} + 35\alpha_{\mathbf{i} + \frac{1}{2} \mathbf{e}^d + \mathbf{e}^{d'}} \right. \\ \left. - 140\alpha_{\mathbf{i} + \frac{1}{2} \mathbf{e}^d} + 63\alpha_{\mathbf{i} + \frac{1}{2} \mathbf{e}^d - \mathbf{e}^{d'}} + 20\alpha_{\mathbf{i} + \frac{1}{2} \mathbf{e}^d - 2\mathbf{e}^{d'}} \right]. \quad (52)$$

Stencil modifications corresponding to a Dirichlet condition at the lower boundary of a coordinate direction are obtained in the obvious way by permuting indices and negating the entries of stencils corresponding to odd order derivatives.

### 3.3 A numerical example

To test the discretization described in the preceding sections, we consider the solution of Poisson's equation in the “D”-shaped annular geometry  $\Omega$  presented in Section IV of [12] and depicted in Figure 4. The mapping  $\mathbf{X}$  from computational coordinates  $\boldsymbol{\xi} = (\xi_1, \xi_2)$  to physical coordinates  $\mathbf{x} = (x_1, x_2)$  is

given by

$$\begin{aligned} x_1 &= 1.7 + [0.074(2\xi_1 - 1) + 0.536] \cos \left[ 2\pi\xi_2 + \sin^{-1}(0.416) \sin(2\pi\xi_2) \right], \\ x_2 &= 1.66 [0.074(2\xi_1 - 1) + 0.536] \sin(2\pi\xi_2), \end{aligned} \quad (53)$$

for  $0 \leq \xi_1, \xi_2 \leq 1$ . We seek the solution of

$$\nabla^2 \Phi(\mathbf{x}) = \rho(\mathbf{x}), \quad \mathbf{x} \in \Omega, \quad (54)$$

satisfying homogeneous Dirichlet boundary conditions in the radial ( $\xi_1$ ) direction

$$\Phi(\mathbf{X}(0, \xi_2)) = \Phi(\mathbf{X}(1, \xi_2)) = 0, \quad 0 \leq \xi_2 \leq 1, \quad (55)$$

and periodic boundary conditions in the azimuthal ( $\xi_2$ ) direction. To test the accuracy of our discretization, we employ a manufactured solution procedure and compute a right-hand side  $\rho$  corresponding to a predetermined, analytically prescribed solution. After forming and solving the linear system resulting from our discretization using the right-hand side so obtained, we can compute the discretization error since the exact solution is known. In particular, we set  $\Phi(\mathbf{x}) = \tilde{\Phi}(\mathbf{X}^{-1}(\mathbf{x}))$ , where

$$\tilde{\Phi}(\xi_1, \xi_2) = 4\xi_1(1 - \xi_1) [1 + 0.1 \sin(8\pi\xi_2)]. \quad (56)$$

Using (56), we apply the divergence theorem to compute the integral of  $\rho$  over a mapped grid cell  $\mathbf{X}(V)$  as

$$\int_{\mathbf{X}(V)} \rho(\mathbf{x}) d\mathbf{x} = \sum_{\pm=+,-} \sum_{d=1}^2 \int_{A_d^\pm} \left( J^{-1} \mathbf{N}^T \mathbf{N} \nabla_{\xi} \tilde{\Phi} \right)_d d\mathbf{A}_{\xi}. \quad (57)$$

Since the mapping (53) is prescribed using simple analytic formulas, the transformation matrix  $\mathbf{N}$  and its Jacobian  $J$  are also explicitly available. The one-dimensional integrals in (57) are evaluated using the DQAG integrator from QUADPACK [13], which implements a globally adaptive Gauss-Kronrod quadrature to prescribed relative and absolute tolerances. For the convergence results presented below, the relative and absolute tolerances were set to  $10^{-12}$  to reduce the quadrature error well below the discretization errors being measured, yielding a nearly exact evaluation of the the integral (57).

The discretization described above was implemented in a test code using the Chombo infrastructure [14]. The resulting linear system was solved using a preconditioned conjugate gradient (PCG) solver from the *Hypre* library [15]. The *Hypre* PCG solver accommodates the  $5 \times 5$  stencil generated by the fourth-order discretization at each grid cell. Given the positive-definite, self-adjoint property of the linear operator, a possible alternative approach would have been to employ a multigrid solver. We do not, however, have a multigrid solver available that can accommodate a  $5 \times 5$  stencil, including the multigrid solvers available in *Hypre*. We therefore employ the *Hypre* PFMG multigrid solver

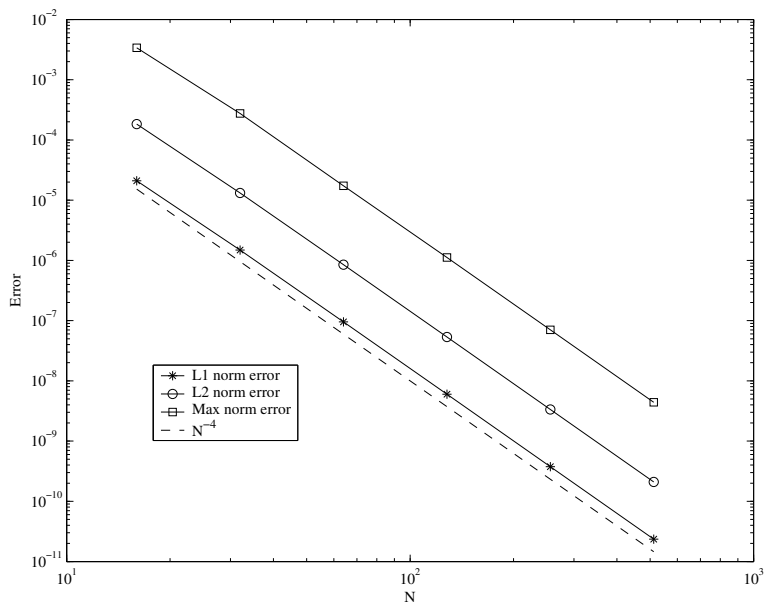


Fig. 5. Test problem convergence study.

applied to a standard second-order discretization of (54) as a preconditioner for CG. Beyond the issue of solver availability, it is generally acknowledged that the combination of a Krylov method with multigrid preconditioning yields a more robust solver, especially with variable coefficients.

Figure 5 shows the  $L_1$ ,  $L_2$  and max norm errors in the discrete solution of (54) using an  $N \times N$  computational grid with  $N = 16, 32, 64, 128, 256$  and  $512$ , plotted against  $N^{-4}$ . By  $L_1$  and  $L_2$  norms, we mean the discrete norms computed using the solution error evaluated at cell centers, rather than continuous norms computed using a reconstruction of the discrete solution over grid cells. The fourth-order convergence rate is clearly observed. In each case the PCG iteration was performed to a tolerance of  $10^{-10}$  on the relative  $L^2$  residual norm (the  $L^2$  norm of the residual relative to that of the right hand side). The multigrid preconditioner was solved to a relative tolerance of  $10^{-2}$  in each iteration. Table 1 shows the relative residual at each iteration together with an estimate of the local convergence rate for the finest grid  $N = 512$ . A pseudocolor plot of the  $N = 512$  solution is shown on the right-hand side of Figure 4.

Iteration number	Convergence rate	Residual norm
1	0.000223	2.232355e-04
2	0.209853	4.684667e-05
3	0.074080	3.470404e-06
4	0.120163	4.170155e-07
5	0.144002	6.005124e-08
6	0.075322	4.523166e-09
7	0.247301	1.118583e-09
8	0.107240	1.199568e-10
9	0.090233	1.082405e-11

Table 1  
PCG convergence rates and residuals for  $N = 512$ .

#### 4 Application to Scalar, Linear Hyperbolic Equations

In this section, we apply the mapped grid formalism to obtain a fourth-order accurate finite-volume discretization of a scalar hyperbolic conservation law

$$\frac{\partial u}{\partial t} + \nabla_{\mathbf{x}} \cdot \mathbf{F} = 0 \quad \text{on} \quad \mathbf{x} \in \Omega \subset \mathbb{R}^D, t \geq 0. \quad (58)$$

This equation expresses the evolution of the conserved scalar field  $u : \Omega \times [0, \infty) \rightarrow \mathbb{R}$  under the action of the vector-valued flux function  $\mathbf{F}(u, \mathbf{x}, t)$ , where  $\mathbf{F} : \Omega \times [0, \infty) \rightarrow \mathbb{R}^D$ . The vector whose entries consist of the wave speeds in each coordinate direction is given by

$$\mathbf{v}(u, \mathbf{x}, t) \equiv \frac{\partial \mathbf{F}}{\partial u}, \quad (59)$$

where  $\mathbf{v} : \Omega \times [0, \infty) \rightarrow \mathbb{R}^D$ . In the simplest case, this velocity vector is a constant.

Because of the ease of formulation for higher-order, we adopt a method-of-lines discretization approach. As in (5), let  $\mathbf{X}$  be a smooth mapping from some abstract Cartesian coordinate space  $\boldsymbol{\xi}$  into physical space. We discretize on a uniform finite-volume grid (1) with grid spacing  $h$ ; thus each control volume is  $V_{\mathbf{i}} = h^D$ . Integrating (58) over a cell  $\mathbf{i}$  and applying (7) and (19)

yields the semi-discrete system of ordinary differential equations

$$\begin{aligned} \frac{d}{dt} \left( \int_{V_i} u J d\xi \right) &= \int_{\mathbf{x}(V_i)} \frac{\partial u}{\partial t} d\mathbf{x} = - \int_{\mathbf{x}(V_i)} \nabla_{\mathbf{x}} \cdot \mathbf{F} d\mathbf{x} \\ &\approx -h^{D-1} \sum_{d=1}^D \left( F_{\mathbf{i}+\frac{1}{2}\mathbf{e}^d}^d - F_{\mathbf{i}-\frac{1}{2}\mathbf{e}^d}^d \right). \end{aligned} \quad (60)$$

Dividing by the uniform cell volume  $h^D$ , equation (60) becomes the fourth-order update formula

$$\frac{d(\overline{uJ})_{\mathbf{i}}}{dt} = -\frac{1}{h} \sum_{d=1}^D \left( F_{\mathbf{i}+\frac{1}{2}\mathbf{e}^d}^d - F_{\mathbf{i}-\frac{1}{2}\mathbf{e}^d}^d \right) + O(h^4), \quad (61)$$

written in terms of the cell-averaged quantity  $\overline{(uJ)}_{\mathbf{i}}$  on the computational grid. The cell average of the solution of the physical space grid is then

$$\tilde{u}_{\mathbf{i}} \equiv \left( \int_{\mathbf{x}(V_i)} d\mathbf{x} \right)^{-1} \int_{\mathbf{x}(V_i)} u(\mathbf{x}) d\mathbf{x} = (\bar{J})_{\mathbf{i}}^{-1} \overline{(uJ)}_{\mathbf{i}}. \quad (62)$$

For discrete conservation, it is easiest to store and to update  $\overline{(uJ)}_{\mathbf{i}}$  directly, converting to  $\tilde{u}_{\mathbf{i}}$  only for output.

#### 4.1 Face-Averaged Flux Approximation

In the update (61), the face-averaged normal interface fluxes  $F_{\mathbf{i}+\frac{1}{2}\mathbf{e}^d}^d$  are approximated to fourth-order by (20). Thus, the problem is reduced to obtaining fourth-order accurate approximations to each component  $s$  of the face-averaged interface fluxes  $\langle F^s \rangle_{\mathbf{i}\pm\frac{1}{2}\mathbf{e}^d}$  ( $s = 1, \dots, D$ ) averaged over the computational space cell faces with normals in the  $d$ -directions ( $d = 1, \dots, D$ ).

Taylor expansion of the integrand of (18) about the center of a  $d$ -th face gives

$$\langle \mathbf{F} \rangle_{\mathbf{i}\pm\frac{1}{2}\mathbf{e}^d} = \mathbf{F}(\xi_{\mathbf{i}\pm\frac{1}{2}\mathbf{e}^d}) + \frac{h^2}{24} \sum_{d' \neq d} \left. \frac{\partial^2 \mathbf{F}}{\partial \xi_{d'}^2} \right|_{\xi=\xi_{\mathbf{i}\pm\frac{1}{2}\mathbf{e}^d}} + O(h^4). \quad (63)$$

Specializing to a linear flux, we assume  $\mathbf{F}(\xi) = \mathbf{v}(\xi)u(\xi)$ . Then (63) becomes

$$\begin{aligned} \langle \mathbf{F} \rangle_{\mathbf{i}\pm\frac{1}{2}\mathbf{e}^d} &= \mathbf{v}_{\mathbf{i}\pm\frac{1}{2}\mathbf{e}^d} u_{\mathbf{i}\pm\frac{1}{2}\mathbf{e}^d}^d \\ &+ \frac{h^2}{24} \sum_{d' \neq d} \left( u \frac{\partial^2 \mathbf{v}}{\partial \xi_{d'}^2} + 2 \frac{\partial \mathbf{v}}{\partial \xi_{d'}} \frac{\partial u}{\partial \xi_{d'}} + \mathbf{v} \frac{\partial^2 u}{\partial \xi_{d'}^2} \right)_{\xi=\xi_{\mathbf{i}\pm\frac{1}{2}\mathbf{e}^d}} + O(h^4), \end{aligned} \quad (64)$$

where we adopt the pointwise notation  $q_{\mathbf{i}\pm\frac{1}{2}\mathbf{e}^d} \equiv q(\xi_{\mathbf{i}\pm\frac{1}{2}\mathbf{e}^d})$ . Thus, the face-averaged flux is expressed in terms of pointwise values of  $\mathbf{v}$ ,  $u$ , and their derivatives at the center of the face  $\mathbf{i}\pm\frac{1}{2}\mathbf{e}^d$ .

The expansion of the integral (63) also gives pointwise values expressed in terms of face-averaged values. Specifically, for pointwise values of  $u$  and  $\mathbf{v}$ , one can write

$$\mathbf{v}_{\mathbf{i}\pm\frac{1}{2}\mathbf{e}^d} = \langle \mathbf{v} \rangle_{\mathbf{i}\pm\frac{1}{2}\mathbf{e}^d} - \frac{h^2}{24} \sum_{d' \neq d} \left. \frac{\partial^2 \mathbf{v}}{\partial \xi_{d'}^2} \right|_{\xi=\xi_{\mathbf{i}\pm\frac{1}{2}\mathbf{e}^d}} + O(h^4), \quad (65a)$$

$$u_{\mathbf{i}\pm\frac{1}{2}\mathbf{e}^d} = \langle u \rangle_{\mathbf{i}\pm\frac{1}{2}\mathbf{e}^d} - \frac{h^2}{24} \sum_{d' \neq d} \left. \frac{\partial^2 u}{\partial \xi_{d'}^2} \right|_{\xi=\xi_{\mathbf{i}\pm\frac{1}{2}\mathbf{e}^d}} + O(h^4). \quad (65b)$$

Thus, the average interface flux is

$$\langle \mathbf{F} \rangle_{\mathbf{i}\pm\frac{1}{2}\mathbf{e}^d} = \langle \mathbf{v} \rangle_{\mathbf{i}\pm\frac{1}{2}\mathbf{e}^d} \langle u \rangle_{\mathbf{i}\pm\frac{1}{2}\mathbf{e}^d} + \frac{h^2}{12} \sum_{d' \neq d} \left( \frac{\partial \mathbf{v}}{\partial \xi_{d'}} \frac{\partial u}{\partial \xi_{d'}} \right)_{\xi=\xi_{\mathbf{i}\pm\frac{1}{2}\mathbf{e}^d}} + O(h^4), \quad (66)$$

written in terms of the face-averages  $\langle u \rangle_{\mathbf{i}\pm\frac{1}{2}\mathbf{e}^d}$  and  $\langle \mathbf{v} \rangle_{\mathbf{i}\pm\frac{1}{2}\mathbf{e}^d}$  and the pointwise values of the gradients of  $u$  and  $\mathbf{v}$  at the center of the face.

In a finite-volume scheme, one works with cell-averaged values. Through the use of primitive functions [16], one can construct face-averages directly in terms of cell averages; at fourth-order on a uniform grid, this yields the centrally-differenced expression

$$\langle q \rangle_{\mathbf{i}\pm\frac{1}{2}\mathbf{e}^d} = \frac{7}{12} (\bar{q}_{\mathbf{i}} + \bar{q}_{\mathbf{i}+\mathbf{e}^d}) - \frac{1}{12} (\bar{q}_{\mathbf{i}+2\mathbf{e}^d} + \bar{q}_{\mathbf{i}-\mathbf{e}^d}) + O(h^4). \quad (67)$$

To approximate the pointwise transverse gradients, we first note that an  $O(h^2)$  approximation is sufficient. In the  $d'$ -th direction, a suitable centrally differenced approximation is

$$\left. \frac{\partial q}{\partial \xi_{d'}} \right|_{\xi=\xi_{\mathbf{i}\pm\frac{1}{2}\mathbf{e}^d}} = \frac{1}{4h} (\bar{q}_{\mathbf{i}+\mathbf{e}^{d'}} + \bar{q}_{\mathbf{i}\pm\mathbf{e}^d+\mathbf{e}^{d'}} - \bar{q}_{\mathbf{i}-\mathbf{e}^{d'}} - \bar{q}_{\mathbf{i}\pm\mathbf{e}^d-\mathbf{e}^{d'}}) + O(h^2). \quad (68)$$

Expressions (67) and (68) provide the approximations necessary to evaluate the face-averaged fluxes (66) to fourth-order given the cell averages of  $u$  and  $\mathbf{v}$  on the computational grid.

To obtain the average  $\bar{u}_{\mathbf{i}}$  from the average  $\overline{(uJ)}_{\mathbf{i}}$ , we again appeal to Taylor series expansion of the integrand to express the average of products as the product of averages:

$$\overline{(uJ)}_{\mathbf{i}} = \bar{u}_{\mathbf{i}} \bar{J}_{\mathbf{i}} + \frac{h^2}{12} (\nabla_{\xi} u \cdot \nabla_{\xi} J)_{\mathbf{i}} + O(h^4). \quad (69)$$

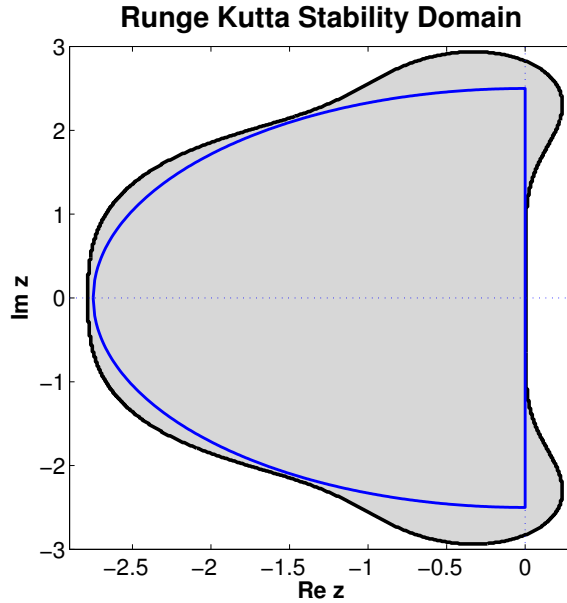


Fig. 6. Stability region of the classical Runge-Kutta scheme. The approximation by a semi-ellipse (77) is shown in blue.

Thus,

$$\bar{u}_i \equiv h^{-D} \int_{V_i} u(\mathbf{x}(\boldsymbol{\xi})) d\boldsymbol{\xi} = (\bar{J})_i^{-1} \left[ (\overline{uJ})_i - \frac{h^2}{12} \nabla_{\boldsymbol{\xi}} u \cdot \nabla_{\boldsymbol{\xi}} J + O(h^4) \right]. \quad (70)$$

We require at least second-order approximations of the gradients and choose the central differences

$$(\nabla_{\boldsymbol{\xi}} u)_i^d = \frac{1}{2h} \left[ \frac{(\overline{uJ})_{i+\mathbf{e}^d}}{\bar{J}_{i+\mathbf{e}^d}} - \frac{(\overline{uJ})_{i-\mathbf{e}^d}}{\bar{J}_{i-\mathbf{e}^d}} \right] + O(h^2) \quad (71)$$

in each direction  $d$ . This choice is freestream preserving; the difference evaluates to zero (within roundoff) provided that the averages are initialized such that, for constant  $u$ ,  $\overline{uJ}_i \equiv u\bar{J}_i$ .

#### 4.2 Time Discretization

As in [7], we discretize the semi-discrete system of ordinary differential equations (61) using the explicit, four-stage, fourth-order classical Runge-Kutta scheme [17]. Consider the variable-coefficient problem

$$\frac{d\mathbf{y}}{dt} = \mathbf{A}(\mathbf{x})\mathbf{y}, \quad (72)$$

where  $\mathbf{y}$  is the vector of  $N$  unknowns  $\overline{(uJ)}_{\mathbf{i}}$  and  $\mathbf{A}(\mathbf{x})$  is an  $N \times N$  spatially-varying variable-coefficient matrix. For all four-stage, fourth-order Runge-Kutta temporal discretizations, the characteristic polynomial is

$$P(z_j) = 1 + z_j + \frac{z_j^2}{2} + \frac{z_j^3}{6} + \frac{z_j^4}{24}, \quad (73)$$

where  $z_j = \Delta t \lambda_j$  and the  $\lambda_j \in \mathbb{C}$  are the  $N$  eigenvalues of  $\mathbf{A}$ . The constant-coefficient stability constraint is

$$|P(z_j)| \leq 1, \quad \forall j \in [1, N]. \quad (74)$$

Alternatively, for all  $j$ , let  $z_j = x_j + iy_j$  with  $x_j, y_j \in \mathbb{R}$ , then the amplification factor  $g_j$  of the fully discrete scheme has real part

$$\operatorname{Re} g_j = \left(1 + x_j + \frac{x_j^2}{2} + \frac{x_j^3}{6} + \frac{x_j^4}{24}\right) - \frac{y_j^2}{2} \left(1 + x_j + \frac{x_j^2}{2}\right) + \frac{y_j^4}{24} \quad (75)$$

and imaginary part

$$\operatorname{Im} g_j = y_j \left(1 + x_j + \frac{x_j^2}{2} + \frac{x_j^3}{6}\right) - \frac{y_j^3}{6} (1 + x_j), \quad (76)$$

and our notion of stability implies that  $|g_j| \leq 1$  for all  $j$ . If one can estimate the eigenvalues of the spatial operator  $\lambda_j$ , one then has a means of selecting a stable timestep. In practice, the semi-ellipse shown in Figure 6,

$$\left(\frac{4x}{11}\right)^2 + \left(\frac{2y}{5}\right)^2 \leq 1 \quad \text{for} \quad x \leq 0, \quad (77)$$

provides a more practical relation to determine stability.

Analytically, the constant-coefficient problem reveals a potential shortcoming of our full discretization. Define the shift operator and its inverse

$$T_d u_{\mathbf{i}} = u_{\mathbf{i}+\mathbf{e}^d} \quad \text{and} \quad T_d^{-1} u_{\mathbf{i}} = u_{\mathbf{i}-\mathbf{e}^d}.$$

The semi-discrete system of ordinary differential equations (61) reduces to

$$\frac{d\overline{(uJ)}_{\mathbf{i}}}{dt} = -\frac{1}{h} \left( \sum_{d=1}^D a_d \left[ \frac{2}{3} (T_d - T_d^{-1}) - \frac{1}{12} (T_d^2 - T_d^{-2}) \right] \right) \overline{(uJ)}_{\mathbf{i}}. \quad (78)$$

On a periodic domain, the eigenvalues are

$$\lambda_{\mathbf{i}} = -\frac{i}{3h} \sum_{d=1}^D a_d \sin \theta_{i_d} [4 - \cos \theta_{i_d}], \quad (79)$$

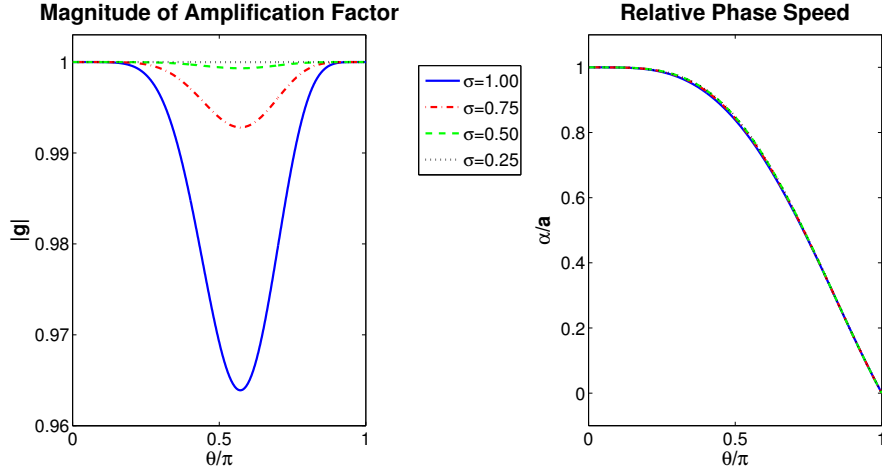


Fig. 7. Variation of the magnitude of the amplification factor  $|g|$  and the relative phase speed  $\alpha/a$  with phase angle  $\theta$  for several values of  $\sigma$ . Note that as  $\theta \rightarrow \pm\pi$ , the damping vanishes and the modes do not propagate. Furthermore, the phase error is effectively independent of  $\sigma$ .

where the discrete phase angles are  $\theta_{i_d} = 2\pi i_d/n$ ,  $i_d = 0, \pm 1, \pm 2, \dots, \pm n/2$ . Because of the central spatial discretization, the eigenvalues are all pure imaginary, that is, the spatial discretization contributes no numerical dissipation. The magnitude of the amplification factor as a function of continuous phase angles is

$$|g| = \sqrt{1 - \frac{y^6}{72} \left(1 - \frac{y^2}{8}\right)}. \quad (80)$$

For  $D = 1$ , this is plotted in Figure 7. Similarly, the relative phase speed of the one-dimensional scheme,

$$\frac{\alpha(\theta)}{a} = -\frac{1}{\sigma\theta} \frac{\text{Im } g(\theta)}{\text{Re } g(\theta)}, \quad (81)$$

where  $\sigma = a\Delta t/h$ , is also plotted in Figure 7. We see that the Runge Kutta scheme adds a small amount of dissipation and that, as  $\theta \rightarrow \pm\pi$ , this dissipation vanishes. At the same time, we see that these high-wavenumber modes (grid modes) do not propagate. For variable-coefficient and nonlinear problems, these undamped grid modes can pollute the solutions, if not cause instability.

### 4.3 Limiting

One approach to stabilize a high-order, no- or low-dissipation scheme for variable-coefficient or nonlinear hyperbolic problems is to add artificial dis-

sipation. For example, adding an artificial dissipation of the form

$$\nu(-1)^{r-1}h^{2r-1}(T-1)^r(1-T^{-1})^r\bar{u}_i, \quad (82)$$

to the discrete scheme in computational space gives a scheme dissipative of order  $2r$  in the sense of Kreiss [18,19]. However, for  $r > 1$ , the discrete higher-order derivatives will introduce new numerical difficulties in the presence of discontinuous solutions or poorly resolved gradients.

An alternative approach from the shock-capturing literature is to use a nonlinear limiting scheme. For linear, variable-coefficient problems, genuinely nonlinear discontinuities (shocks) do not occur. However, velocity gradients can cause slopes in the solution to steepen, and initial and boundary conditions can introduce linear discontinuities. We therefore will use nonlinear flux limiting for robust handling of under-resolved gradients and discontinuities. A disadvantage of this approach is that it locally reduces the order of convergence of the scheme, but for smooth problems, this should only occur in a very small subset of cells, if at all. Thus, the maximum pointwise error may not converge at fourth-order, but the errors should converge near fourth-order almost everywhere.

In the mapped-grid formalism, we propose to apply a limiter scheme to the cell-averaged solution on the computational grid,  $\bar{u}_i$ . As a specific example, we implement a method-of-lines variant of the recently-improved, extremum-preserving limiter developed in [8]. In this implementation, the upwind of the two limited face values at each face of the computational grid is chosen as the basis state of the flux for each right-hand side evaluation of the time integrator. The only modification to the original scheme specific to mapped grids is that the upwind direction at each face is determined using the normal velocity on the computational mesh, that is,  $\mathbf{w} = \mathbf{N}^T \mathbf{v}$ . We use the recommended limiter coefficient  $C = 1.25$ .

For the smooth-data initial value problems considered in the next section, this limiting procedure achieves fourth-order convergence on mapped grids with sufficient resolution. However, we have identified some smooth problems for which this specific limiter fails to produce the optimal convergence rate as the mesh is refined. The cause of this sub-optimal convergence is not completely understood. It does not appear that the issue is a reflection of the approach to limiting within the mapped grid framework but instead is a result of the specific combination of the limiter and discretizations used. The subject of a robust limiter for the mapped grid formalism is still an open issue and is the subject of ongoing investigation.

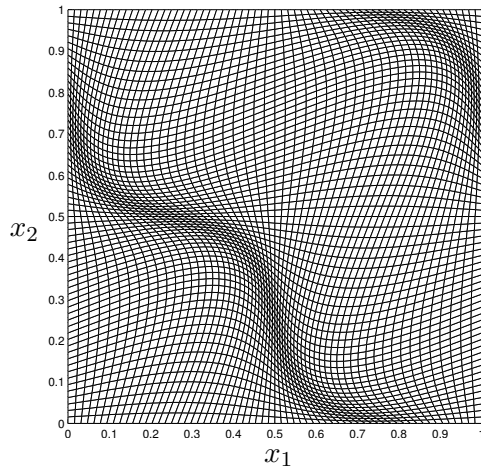


Fig. 8. The deformed mesh (84) used in the example problems, shown with  $N=64$  cells in each direction.

#### 4.4 Example Problems

To demonstrate the behavior of the hyperbolic mapped finite-volume scheme, we investigate several initial value test problems. On a periodic domain, we consider uniform advection of constant, sinusoidal, and compactly supported initial data. We also consider the standard limiter test problem of rotational advection of a slotted cylinder. For each of these problems, we compute on a uniform, Cartesian mesh and a nonlinearly deformed mesh.

For each smooth problem, a grid convergence study is conducted. We compute on a sequence of six meshes with  $N = \{16, 32, 64, 128, 256, 512\}$ . The error in the cell-averaged numerical solution  $\tilde{u}_i$  is computed by differencing with a cell-averaged reference solution. The exact solutions for the test problems are easily expressed pointwise, but to compute the cell-averaged reference solution on the mapped grid analytically is difficult. Instead, for our reference solution, we compute cell-centered pointwise values  $(uJ)_i$  on a uniform computational grid with  $h = 1/8N$ , and then use the relationships (4) and (62) to obtain approximate values of  $\tilde{u}_i$  on the original, coarser grid. Thus, our reference solution is a fourth-order approximation of the cell-averaged exact solution, but for the problems we consider, this error in the reference solution is several orders of magnitude smaller than the error between the computed solution and the reference solution.

$L_\infty$  Error Norm for Base Scheme

$N_{\text{cells}}$	16	32	64	128	256	512
Cartesian	0.00e+00	0.00e+00	0.00e+00	0.00e+00	0.00e+00	0.00e+00
Deformed	0.00e+00	0.00e+00	0.00e+00	0.00e+00	4.44e-16	2.22e-16

Table 2

Maximum pointwise errors for freestream preservation test at six resolutions for the base scheme.

$L_\infty$  Error Norm for Base Scheme with Limiter

$N_{\text{cells}}$	16	32	64	128	256	512
Cartesian	0.00e+00	0.00e+00	0.00e+00	0.00e+00	0.00e+00	0.00e+00
Deformed	1.11e-16	2.22e-16	3.33e-16	6.66e-16	2.44e-15	4.13e-13

Table 3

Maximum pointwise errors for freestream preservation test at six resolutions for the base scheme with limiter.

#### 4.4.1 Mappings

For reference, we compute on a uniform, Cartesian mesh, which corresponds to the identity mapping

$$\mathbf{x}(\boldsymbol{\xi}) = \boldsymbol{\xi}. \quad (83)$$

This demonstrates that the metric computations reduce to the correct trivial relationships and provides a baseline against which to compare the results of simulations with less trivial mappings.

The nonlinear mapping we consider is a specialization of the mapping used in [20]. This mapping is generated by perturbing a uniform Cartesian mesh by a Cartesian sinusoidal product, specifically,

$$x_d = \xi_d + \alpha_d \prod_{p=1}^D \sin(2\pi\xi_p), \quad d = 1, \dots, D. \quad (84)$$

To ensure that the perturbed mesh does not tangle, it is sufficient to take  $\forall d$ ,  $0 \leq 2\pi\alpha_d \leq 1$ . This mapping cannot be inverted analytically, however, noting that

$$\xi_d = x_d + \frac{\alpha_d}{\alpha_{d'}}(x_{d'} - x_d), \quad d = 1, \dots, D, \quad d \neq d', \quad (85)$$

for  $\alpha_{d'} \neq 0$ , the mapping can be inverted numerically using a fixed-point iteration on the scalar equation (84) for  $\xi_{d'}$ . Note that for this mapping, the Jacobian is not constant. A depiction of the mapped grid for  $N = 64$  in each direction is plotted in Figure (8).

#### 4.4.2 Uniform Advection of Constant Data

We consider uniform advection of constant initial data on a periodic domain  $\mathbf{x} \in [0, 1)^2$ . The initial conditions are

$$u_0(\mathbf{x}) = 1, \tag{IC1}$$

and the uniform velocity vector is

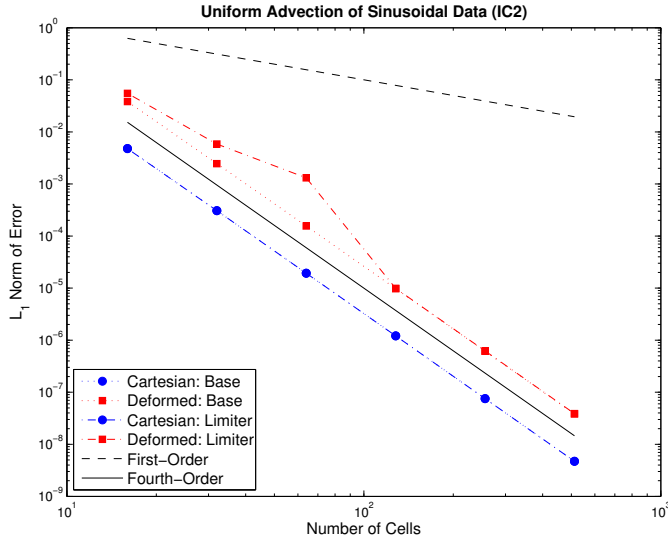
$$\mathbf{v}(\mathbf{x}) = (1, 0.5). \tag{86}$$

The exact solution is  $u(\mathbf{x}, t) = 1$  at all times; we take a constant nominal CFL number of  $\sigma = v_1 \Delta t N = 0.32$  and integrate to a final time of  $t = 2$ . While this problem appears to be trivial, it is an important demonstration of the freestream preservation capability of the discretization.

Results of grid convergence studies are presented in Tables 2 and 3. Freestream preservation is demonstrated by the fact that the maximum pointwise error in the computed solution in both cases is at most dominated by round-off error. Both with and without the limiter, the method is shown to be freestream preserving.

We note that the results differ with and without the limiter because the limiter scheme operates on data even when the solution is constant. The limiter never reduces the order of the scheme in this case, but the method does a number of finite-precision operations that can introduce additional round-off error. This is particularly true on the deformed mesh (84); note that the non-constant Jacobian for this mapping also contributes to round-off error. The magnitude of round-off error increases with the number of cells because more time steps, and hence more floating-point operations, are required to reach the final time.

If one were so inclined, a small modification to the limiter algorithm can be made to prohibit it from acting on digits with dubious significance. Specifically, the first step in constructing face values and in constructing parabolic interpolants is to compute a pair of differences between face and cell values. If the maximum relative magnitude of the two differences is above some small value (say  $10^{-15}$ ), the limiter algorithm proceeds normally; otherwise, the limiting process is skipped. In practice, this produces limited freestream-test results identical to those for the base scheme (Table 2) with no apparent effect on limiter performance for less trivial applications.



$L_1$  Error Norm for Base Scheme

$N_{\text{cells}}$		16	32	64	128	256	512
Cartesian	error	4.81e-03	3.07e-04	1.93e-05	1.21e-06	7.55e-08	4.72e-09
	rate	-	3.97	3.99	4.00	4.00	4.00
Deformed	error	3.82e-02	2.45e-03	1.56e-04	9.79e-06	6.13e-07	3.83e-08
	rate	-	3.96	3.97	3.99	4.00	4.00

$L_1$  Error Norm for Base Scheme with limiter

$N_{\text{cells}}$		16	32	64	128	256	512
Cartesian	error	4.75e-03	3.07e-04	1.93e-05	1.21e-06	7.55e-08	4.72e-09
	rate	-	3.95	3.99	4.00	4.00	4.00
Deformed	error	5.49e-02	5.86e-03	1.31e-03	9.85e-06	6.21e-07	3.89e-08
	rate	-	3.23	2.16	7.06	3.99	4.00

Fig. 9. Convergence of maximum pointwise error with grid refinement for uniform advection (86) of sinusoidal data (IC2) for both meshes.

#### 4.4.3 Uniform Advection of Sinusoidal Data

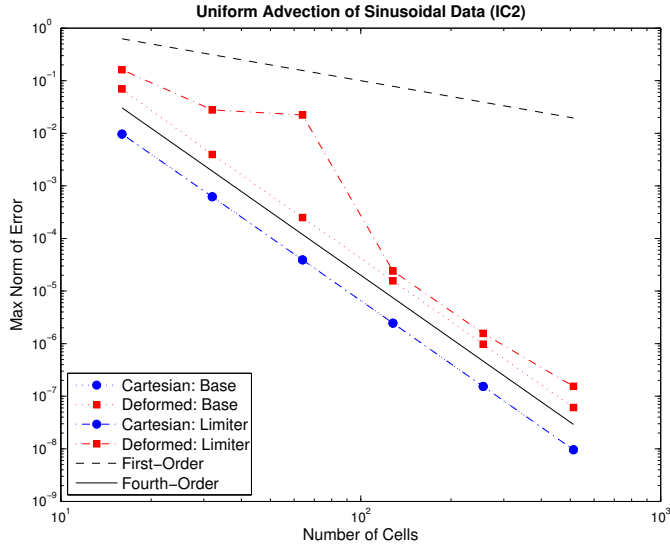
We consider uniform advection of Cartesian-product sinusoidal initial data on a periodic domain  $\mathbf{x} \in [0, 1]^2$ . The initial conditions are

$$u_0(\mathbf{x}) = \cos(2\pi x_1) \cos(2\pi x_2), \quad (\text{IC2})$$

and the uniform velocity vector is again (86). The exact solution is

$$u(\mathbf{x}, t) = u_0(\mathbf{x} - \mathbf{v}t), \quad (87)$$

where  $u_0$  is by definition periodic in each direction with unit period. Again, we take a constant CFL of  $\sigma = 0.32$  and integrate to final time of  $t = 2$ .



$L_\infty$  Error Norm for Base Scheme

$N_{\text{cells}}$		16	32	64	128	256	512
Cartesian	error	9.59e-03	6.22e-04	3.92e-05	2.46e-06	1.54e-07	9.60e-09
	rate	-	3.95	3.99	3.99	4.00	4.00
Deformed	error	6.97e-02	3.94e-03	2.49e-04	1.56e-05	9.77e-07	6.11e-08
	rate	-	4.14	3.98	4.00	4.00	4.00

$L_\infty$  Error Norm for Base Scheme with limiter

$N_{\text{cells}}$		16	32	64	128	256	512
Cartesian	error	9.70e-03	6.22e-04	3.92e-05	2.46e-06	1.54e-07	9.60e-09
	rate	-	3.96	3.99	3.99	4.00	4.00
Deformed	error	1.61e-01	2.78e-02	2.23e-02	2.41e-05	1.57e-06	1.55e-07
	rate	-	2.53	0.32	9.85	3.94	3.34

Fig. 10. Convergence of maximum pointwise error with grid refinement for uniform advection (86) of sinusoidal data (IC2) for both meshes.

Results of grid convergence studies are plotted in Figures 9 and 10. For the unlimited scheme, fourth-order convergence is seen for both meshes. Fourth-order convergence is also obtained by the limited scheme for the Cartesian grid; in fact the errors are nearly identical to the unlimited scheme.

However, on the deformed mesh (84), fourth-order convergence is not in general seen for the limited scheme. At a resolution of  $N = 64$ , large *isolated* errors occur, as is indicated by the large difference in  $L_1$  and  $L_\infty$  norm behaviors. However, at finer resolutions, near-fourth-order convergence is again obtained for this mapping. The isolated errors occur in the regions of most strongly stretched mesh, and the isolated behavior at  $N = 64$  suggests a transition in the detail of the mapped grid that can be represented at finite resolution.

Note that, in computational space, the problem is a variable-coefficient problem on a uniform mesh, where the solution is locally modified by the Jacobian. Around  $N = 64$ , enough detail of the mapping is represented such that, in isolated regions, some variations in the velocity and/or solution are identifiable but under-resolved. Thus, the limiter attempts to control the solution in these regions, causing the scheme to drop order. As the mesh is refined, the variations are resolved, and the number of points at which the limiter is active drops. The good agreement between the limited and unlimited  $L_1$  error norms at resolutions finer than  $N = 64$  supports this explanation.

#### 4.4.4 Uniform Advection of Compactly-Supported Data

We consider uniform advection of compactly-supported smooth initial pulse on a periodic domain  $\mathbf{x} \in [0, 1)^2$ . The initial conditions are

$$u_0(\mathbf{x}) = \begin{cases} \cos^8\left(\frac{\pi r}{2R}\right), & 0 \leq r \leq R, \\ 0, & \text{otherwise,} \end{cases} \quad (\text{IC3})$$

$r = |\mathbf{x} - \mathbf{x}^*|$ , and the uniform velocity vector is again (86). We take  $R = 0.25$  and  $\mathbf{x}^* = (0.75, 0.5)$ . The exact solution is again given by (87), with  $u(\mathbf{x} + \mathbf{e}^d, t) = u(\mathbf{x}, t)$  for  $d = 1, 2$ . We take a constant CFL of  $\sigma = 0.32$  and take the final time to be  $t = 2$ .

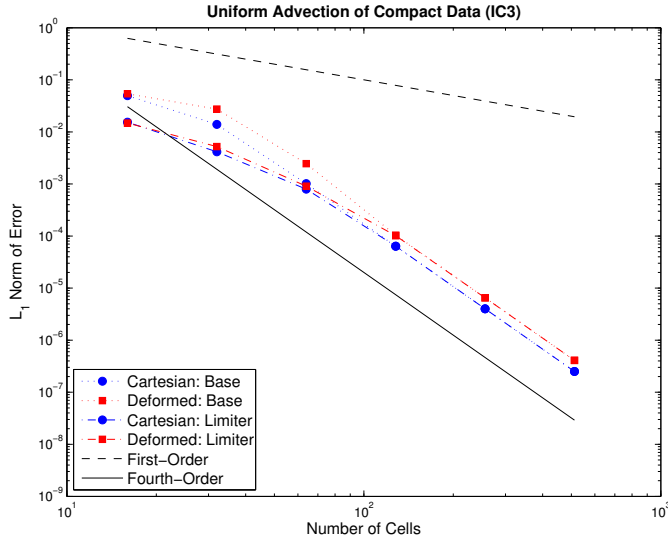
Results of the grid convergence study for the base and the limited scheme are plotted in Figures 11 and 12. For both schemes and both meshes, the compact function is poorly represented at coarse resolutions; at  $N = 16$ , there are only four cells in each direction across the non-zero portion of the function. By around  $N = 128$ , the error behavior begins to enter the asymptotic regime for both norms, and the computed solution converges at a fourth-order rate for both schemes and on both meshes.

#### 4.4.5 Circular Advection of a Slotted Cylinder

A standard problem used to test the multidimensional performance of limiting schemes is the circular advection of a slotted cylinder. The rotational velocity vector for rotation about  $\mathbf{x}^c = (0.5, 0.5)$  is

$$\mathbf{v}(\mathbf{x}) = 2\pi\omega(-(x_2 - x_2^c), (x_1 - x_1^c)), \quad (\text{V3})$$

where we take  $\omega = 1$ . We define a slotted cylinder of radius  $R = 0.15$ , slot width  $W = 0.05$ , and slot height  $H = 0.25$  centered on  $\mathbf{x}^* = (0.5, 0.75)$  for the



$L_1$  Error Norm for Base Scheme

$N_{\text{cells}}$		16	32	64	128	256	512
Cartesian	error	4.95e-02	1.39e-02	1.01e-03	6.35e-05	4.00e-06	2.51e-07
	rate	-	1.83	3.78	3.99	3.99	3.99
Deformed	error	5.38e-02	2.74e-02	2.45e-03	1.04e-04	6.52e-06	4.10e-07
	rate	-	0.97	3.48	4.56	4.00	3.99

$L_1$  Error Norm for Base Scheme with limiter

$N_{\text{cells}}$		16	32	64	128	256	512
Cartesian	error	1.54e-02	4.15e-03	7.95e-04	6.38e-05	4.00e-06	2.51e-07
	rate	-	1.89	2.38	3.64	4.00	3.99
Deformed	error	1.48e-02	5.22e-03	9.05e-04	1.01e-04	6.51e-06	4.10e-07
	rate	-	1.50	2.53	3.16	3.96	3.99

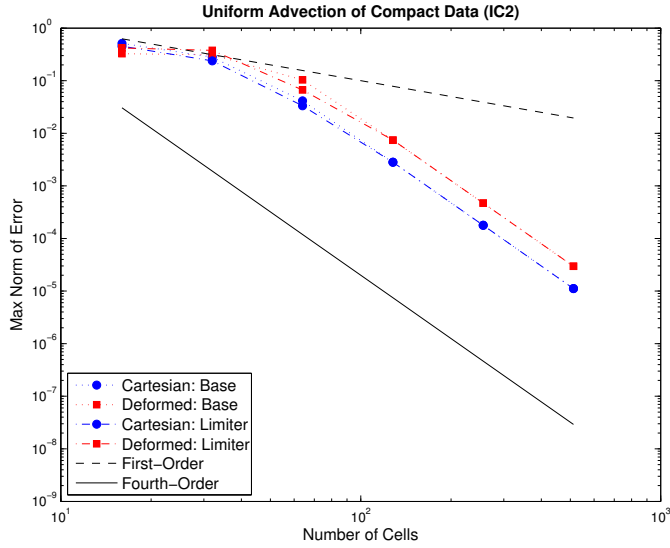
Fig. 11. Convergence of  $L_1$  error norm with grid refinement for the base and limited schemes for uniform advection (86) of compactly-supported data (IC3) for both meshes.

initial conditions:

$$u_0(\mathbf{x}) = \begin{cases} 0, & 0 \leq R < r, \\ 0, & |2z_1| < W \quad \text{and} \quad 0 < z_2 + R < H, \\ 1, & \text{otherwise,} \end{cases} \quad (\text{IC4})$$

where  $\mathbf{z} = \mathbf{x} - \mathbf{x}^*$  and  $r = |\mathbf{z}|$ . We simulate on the truncated domain  $\mathbf{x} \in [0, 1]^2$  with  $N = 100$  cells in each direction. The exact solution at time  $t = 1$  is the initial condition, and we use a fixed time step of  $\Delta t = 1.59236 \times 10^{-3}$ .

The initial and final solution for simulation on a Cartesian mesh are plotted



$L_\infty$  Error Norm for Base Scheme

$N_{\text{cells}}$		16	32	64	128	256	512
Cartesian	error	5.12e-01	2.81e-01	4.14e-02	2.81e-03	1.78e-04	1.12e-05
	rate	-	0.87	2.76	3.88	3.98	4.00
Deformed	error	3.26e-01	3.11e-01	1.04e-01	7.38e-03	4.70e-04	2.96e-05
	rate	-	0.07	1.59	3.81	3.97	3.99

$L_\infty$  Error Norm for Base Scheme with limiter

$N_{\text{cells}}$		16	32	64	128	256	512
Cartesian	error	4.52e-01	2.38e-01	3.33e-02	2.82e-03	1.78e-04	1.12e-05
	rate	-	0.93	2.84	3.56	3.98	4.00
Deformed	error	4.19e-01	3.77e-01	6.66e-02	7.44e-03	4.70e-04	2.96e-05
	rate	-	0.15	2.50	3.16	3.98	3.99

Fig. 12. Convergence of maximum pointwise error with grid refinement for the base and limiter schemes for uniform advection (86) of compactly-supported data (IC3) on both meshes.

in Figure 13. The basic shape of the cylinder is preserved, albeit with some spreading of the initially sharp edges of the cylinder. The slot has some fill-in, but the shape and size of the slot is fairly well preserved. This is a very good approximation for such a coarse resolution; note that there are only five cells across the slot.

The initial and final solution for simulation on the mapped grid (84) are plotted in Figure 14. Again, the basic shape of the cylinder is preserved, although there is more smearing than for the Cartesian case. In addition, note that there are slightly larger overshoots (still only 1%) than for the Cartesian case. The symmetry of the cylinder is still relatively good, despite the distortions

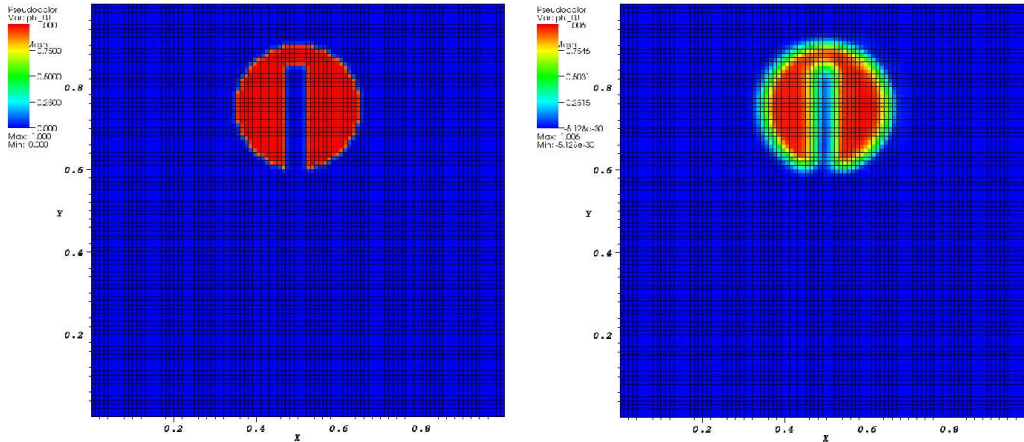


Fig. 13. Circular advection of a slotted cylinder on a  $100 \times 100$  Cartesian grid. The left is the initial condition (and reference solution), and the right is the computed solution after one revolution. The slot and bridge do fill in and slump, respectively, but the overall agreement is good.

in the mesh.

## 5 Summary

We have presented a strategy for the construction of high-order, finite-volume discretizations of flux divergences in mapped coordinates. The approach is based on the systematic development of sufficiently accurate cell face averages, including the computation of product averages in terms of factor averages

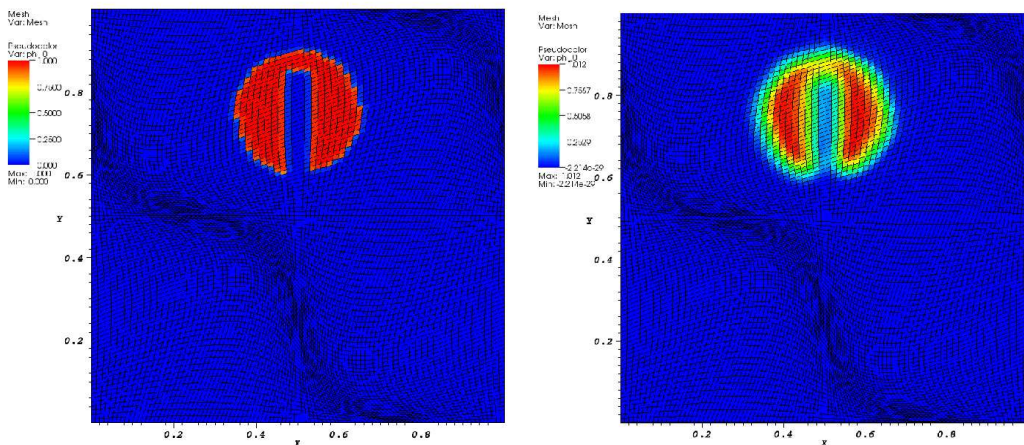


Fig. 14. Circular advection of a slotted cylinder on a  $100 \times 100$  deformed grid (84). The left is the initial condition (and reference solution), and the right is the computed solution after one revolution. The slot and bridge do fill in and slump, respectively, but the overall agreement is good.

and/or face-centered values. Among the face averages to be computed are those of the coordinate mapping metric factors, whose calculation affects not only the overall accuracy of the scheme but also freestream preservation. The latter is automatically achieved to machine roundoff by representing the metric factors as exterior derivatives, whose face averages are in turn reduced to quadratures on face hyperedges. The quadratures can be performed by any convenient method of sufficient accuracy.

To demonstrate the approach, we developed fourth-order discretizations of prototypical elliptic and hyperbolic problems. In addition to testing fourth-order accuracy, the elliptic example displayed the use of an operator based on a second-order finite-volume discretization as a preconditioner in a conjugate gradient iteration. Such strategies can be important in reducing the solver cost of the larger stencils that inevitably accompany high-order discretizations. In the hyperbolic examples, we included an improved nonlinear limiter [8]. Our results indicate that the limited method can achieve a fourth-order convergence rate for smooth data on mapped grids and can control oscillations for discontinuous data on mapped grids.

Although we focused on fourth-order, finite-volume discretizations in this paper, higher-order discretizations are obtainable by a similar strategy. The essential ingredients are a generalization of the cell face average product formula (17), more accurate quadrature formulas for the integrals of metric factors over face hyperedges in (11), and a discretization of flux face averages to the desired order of accuracy. Further extensions include moving mapped grids, as well as generalization from domains describable by a smooth mapping from a single Cartesian computational grid to more complicated multiblock geometries.

## References

- [1] M. Vinokur, An analysis of finite-difference and finite-volume formulations of conservation laws, *J. Comput. Phys.* 81 (1989) 1–52.
- [2] D. Calhoun, R. J. LeVeque, An accuracy study of mesh refinement on mapped grids, in: T. Plewa (Ed.), *Adaptive Mesh Refinement - Theory And Applications: Proceedings of The Chicago Workshop On Adaptive Mesh Refinement Methods*, Vol. 41 of *Lecture Notes in Computational Science and Engineering*, Springer Verlag, 2003, pp. 91–102.
- [3] D. A. Calhoun, C. Helzel, R. J. Leveque, Logically rectangular grids and finite volume methods for PDEs in circular and spherical domains, *SIAM Rev.* 50 (4) (2008) 723–752.
- [4] M. Barad, P. Colella, A fourth-order accurate local refinement method for Poisson’s equation, *J. Comput. Phys.* 209 (2005) 1–18.

- [5] P. D. Thomas, C. K. Lombard, Geometric conservation law and its application to flow computations on moving grids, *AIAA J.* 17 (10) (1979) 1030–1037.
- [6] D. A. Kopriva, Metric identities and the discontinuous spectral element method on curvilinear meshes, *SIAM J. Sci. Comput.* 26 (3) (2006) 301–327.
- [7] M. R. Visbal, D. V. Gaitonde, On the use of high-order finite-difference schemes on curvilinear and deforming meshes, *J. Comput. Phys.* 181 (1) (2002) 155–185.
- [8] P. Colella, M. D. Sekora, A limiter for PPM that preserves accuracy at smooth extrema, *J. Comput. Phys.* 227 (2008) 7069–7076.
- [9] M. Spivak, *Calculus on Manifolds*, W. A. Benjamin, Inc., New York, NY, 1965.
- [10] C. H. Evans, J. H. Hawley, Simulation of magnetohydrodynamic flows - a constrained transport method, *Astrophysical Journal* 332 (1988) 659.
- [11] J. B. Bell, P. Colella, J. A. Trangenstein, M. Welcome, Adaptive mesh refinement on moving quadrilateral grids, in: *Proceedings, 9th AIAA Computational Fluid Dynamics Conference*, Buffalo, NY, 1989, pp. 471–479, aIAA-1989-1979.
- [12] R. L. Miller, M. S. Chu, J. M. Greene, Y. R. Lin-Liu, R. E. Waltz, Noncircular, finite aspect ratio, local equilibrium model, *Phys. Plasmas* 5 (4) (1998) 973–978.
- [13] <http://www.netlib.org/quadpack/>.
- [14] P. Colella, D. T. Graves, T. J. Ligocki, D. F. Martin, D. Modiano, D. B. Serafini, B. V. Straalen, Chombo Software Package for AMR Applications - Design Document, <http://seesar.lbl.gov/anag/chombo>.
- [15] <http://computation.llnl.gov/casc/hypre>.
- [16] P. Colella, P. R. Woodward, The Piecewise Parabolic Method (PPM) for gas-dynamical simulations, *J. Comput. Phys.* 54 (1) (1984) 174–201.
- [17] J. D. Lambert, *Numerical Methods for Ordinary Differential Systems*, John Wiley & Sons, New York, 1991.
- [18] R. D. Richtmyer, K. W. Morton, *Difference Methods for Initial-Value Problems*, 2nd Edition, John Wiley & Sons, New York, 1967.
- [19] B. Gustafsson, H.-O. Kreiss, J. Oliger, *Time Dependent Problems and Difference Methods*, Pure and Applied Mathematics, John Wiley & Sons, New York, 1995.
- [20] P.-O. Persson, J. Bonet, J. Peraire, Discontinuous Galerkin solution of the Navier-Stokes equations on deformable domains, *Comput. Methods Appl. Mech. Eng.* 198 (2009) 1585–1595.